LUND UNIVERSITY

Mechanical properties of transmutation-induced precipitates in tungsten

An ab initio study

Vesti, Anders

2025

Document Version:
Publisher's PDF, also known as Version of record

Link to publication

Citation for published version (APA):
Vesti, A. (2025). *Mechanical properties of transmutation-induced precipitates in tungsten: An ab initio study*. [Doctoral Thesis (compilation), Department of Industrial and Mechanical Sciences]. Lund University.

Total number of authors:
1

General rights
Unless other specific re-use rights are stated the following general rights apply:
Copyright and moral rights for the publications made accessible in the public portal are retained by the authors and/or other copyright owners and it is a condition of accessing publications that users recognise and abide by the legal requirements associated with these rights.
• Users may download and print one copy of any publication from the public portal for the purpose of private study or research.
• You may not further distribute the material or use it for any profit-making activity or commercial gain
• You may freely distribute the URL identifying the publication in the public portal

Read more about Creative commons licenses: https://creativecommons.org/licenses/

Take down policy
If you believe that this document breaches copyright please contact us providing details, and we will remove access to the work immediately and investigate your claim.

LUND UNIVERSITY

PO Box 117
221 00 Lund
+46 46-222 00 00

Download date: 17. Aug. 2026

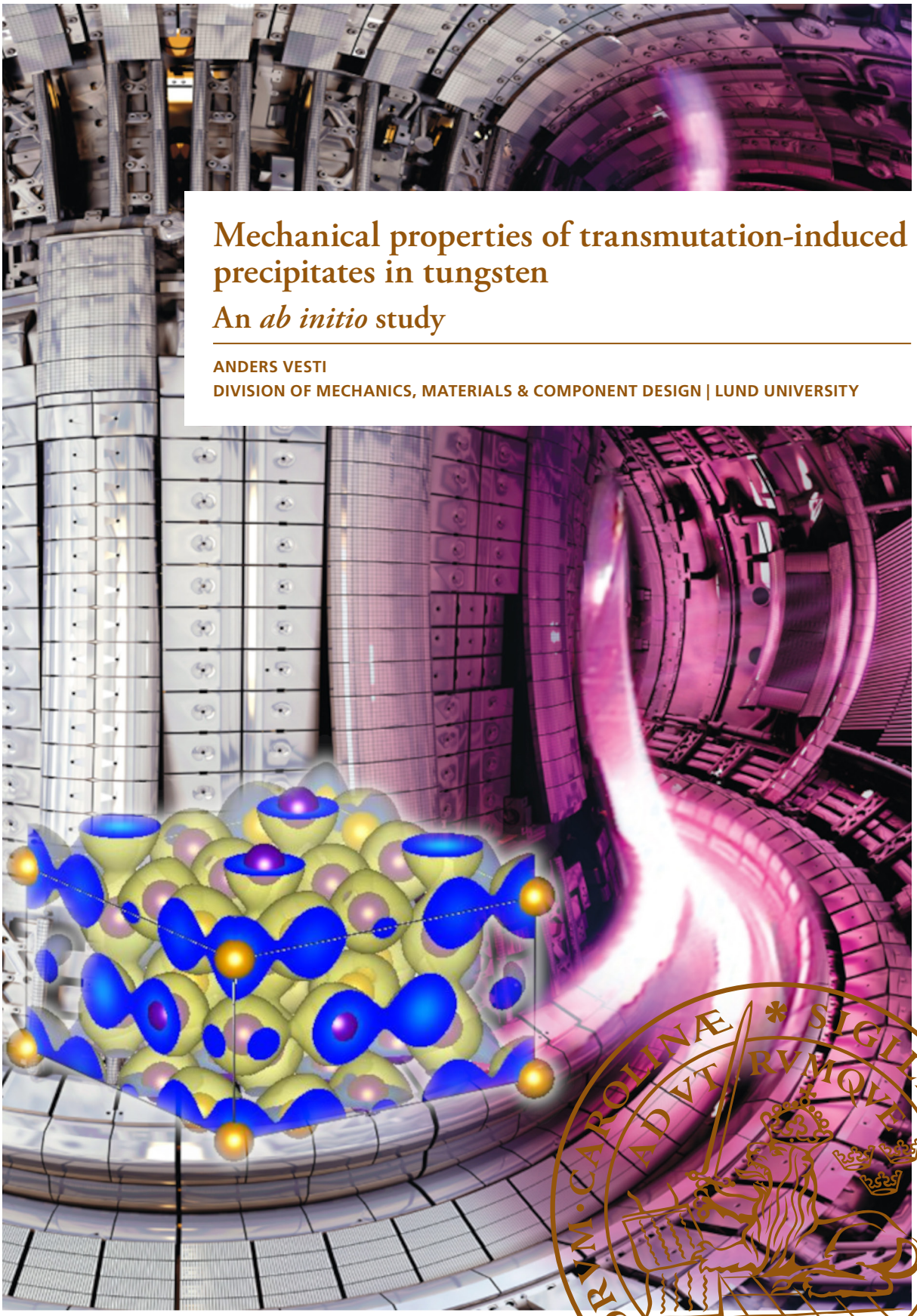

Mechanical properties of transmutation-induced precipitates in tungsten

An *ab initio* study

ANDERS VESTI
DIVISION OF MECHANICS, MATERIALS & COMPONENT DESIGN | LUND UNIVERSITY

Printed by Media-Tryck, Lund 2025 NORDIC SWAN ECOLABEL 3041 0903

Faculty of Engineering, LTH
Department of Industrial and Mechanical Sciences
Division of Mechanics, Materials & Component Design

ISBN 978-91-8104-489-8

Mechanical properties of transmutation-induced precipitates in tungsten

Mechanical properties of transmutation-induced precipitates in tungsten

An *ab initio* study

by Anders Vesti

LUND
UNIVERSITY

Thesis for the degree of Doctorate
Thesis advisors: Dr. Pär A. T. Olsson, Prof. Solveig Melin
Faculty opponent: Dr. Prof. Miroslav Černý

To be presented, with the permission of the Division of Mechanics, Materials & Component Design of Lund University, for public criticism in the M:J lecture hall (2nd floor, M-huset) at the Department of Industrial and Mechanical Sciences on Friday, September 12th 2025 at 09:00.

Organization	Document name
LUND UNIVERSITY Department of Industrial and Mechanical Sciences Box 118, SE–221 00 LUND, Sweden	**DOCTORAL DISSERTATION** Date of disputation 2025-09-12 Sponsoring organization
Author(s) Anders Vesti	

Title and subtitle

Mechanical properties of transmutation-induced precipitates in tungsten: An *ab initio* study

Abstract

This study explores the intrinsic properties of irradiation-induced W–Re and W–Os σ and χ phases using first-principles calculations. Structural stability, elasticity, fracture properties, and thermal expansion behavior were analyzed.

Using the sublattice model, site occupancy and formation enthalpies were determined, showing that Re and Os preferentially occupy low-coordination sites, with Os exhibiting a stronger ordering tendency. The W–Re χ phase is stable at 0 K, while calculations of the free energy indicate thermally induced stability of the σ phase at 1050 K for W–Re and 130 K for W–Os. Dynamic stability of the σ phase depends on the transmutation product concentration and Wyckoff site occupation, with instability occurring above 73 at.% Re in W–Re and 53 at.% Os in W–Os. An unstable vibrational mode in W–Os leads to a transformation into an orthorhombic phase.

The thermal expansion coefficient was determined for the W–Re phases, revealing a significant mismatch with the W matrix, particularly for precipitates of the χ-type. The mismatch can induce thermal stresses, potentially compromising the durability of W-based components under cyclic thermal loading.

These findings support the concern that σ and χ precipitates may amplify the brittle nature of W and require further investigation to assess their impact on the longevity of W-based components.

Key words

Tungsten, rhenium, osmium, DFT, precipitation, σ, χ, Frank-Kasper phases

Classification system and/or index terms (if any)

Supplementary bibliographical information	Language
	English
ISSN and key title	ISBN
	978-91-8104-489-8 (print) 978-91-8104-490-4 (pdf)
Recipient's notes	Number of pages: 123 / Price
	Security classification

I, the undersigned, being the copyright owner of the abstract of the above-mentioned dissertation, hereby grant to all reference sources the permission to publish and disseminate the abstract of the above-mentioned dissertation.

Signature Date: 2025-08-11

DOKUMENTDATABLAD enl SIS 61 41 21

Mechanical properties of transmutation-induced precipitates in tungsten

An *ab initio* study

by Anders Vesti

LUND
UNIVERSITY

Cover illustration front: The vacuum chamber of the ITER reactor with the unit cell of σ phase superimposed.

Funding information: The thesis work was financially supported by the Swedish Research Council through grants No. 2016-04162, No. 2018-04348 and No. 2022-04497.

© Anders Vesti 2025

Division of Mechanics, Materials & Component Design, Department of Industrial and Mechanical Sciences

ISBN: 978-91-8104-489-8 (print)
ISBN: 978-91-8104-490-4 (pdf)

Printed in Sweden by Media-Tryck, Lund University, Lund 2025

Media-Tryck is a Nordic Swan Ecolabel certified provider of printed material. Read more about our environmental work at www.mediatryck.lu.se

MADE IN SWEDEN

Dedicated to my family
Erik – Nina – Rasmus

And my love
Jiabao

Contents

List of publications

This thesis is based on the following publications, referred to by their Roman numerals:

I ***Ab-initio* investigation of mechanical and fracture-related properties of W–Re σ and χ precipitates**
A. Vesti, P. Hiremath, S. Melin, P.A.T. Olsson
Journal of Nuclear Materials 557 (2023) 154261

II **First-principles study on thermal expansion of W–Re sigma and chi phases**
A. Vesti, D. Music, P.A.T. Olsson
Nuclear Materials and Energy 39 (2024) 101684

III **Impact of composition and lattice site occupancy on mechanical stability and fracture-related properties in W-Os sigma phase**
A. Vesti, D. Music, T. Hammerschmidt, M. Palumbo, P.A.T. Olsson
Scientific Reports (under review)

IV **First-principles study of dynamic instability and phase transformation in the W–Re and W–Os sigma phase**
A. Vesti, D. Music, T. Hammerschmidt, M. Palumbo, P.A.T. Olsson
Physical Review Materials 9 (2025) 063602

All papers are reproduced with permission of their respective publishers.

List of Acronyms

BCC body-centered cubic

CTE coefficient of thermal expansion

DFT Density Functional Theory

DG Debye-Grüneisen

EDOS electron density of states

GGA generalized gradient approximation

HCP hexagonal close-packed

ITER International Thermonuclear Experimental Reactor

JET Joint European Torus

MD molecular dynamics

PAW projector augmented wave

PDOS phonon density of states

PFC plasma-facing components

QHA quasi-harmonic approximation

Acknowledgements

First and foremost, I extend my sincere gratitude to Dr. Pär A. T. Olsson for his guidance and patience throughout my Ph.D. journey. Regardless of the time or circumstances, he has always been generous with his support and insights. I am truly grateful for the opportunity to pursue my doctoral studies under his supervision.

I would also like to express my sincere appreciation to Prof. Solveig Melin for sharing her expertise and continuing to take an active interest in my work even after her retirement. Additionally, I am thankful to Dr. Per Hansson for his assistance in the early stages of my Ph.D. and for introducing me to the courses where I served as a teaching assistant.

A special thanks goes to Prof. Denis Music from Malmö University, his guidance was instrumental in shaping several of the papers of this thesis; to Prof. Thomas Hammerschmidt from Ruhr-Universität Bochum, whose exceptional knowledge greatly influenced the development of Papers III and IV; and to Dr. Mauro Palumbo from the University of Turin for his valuable insights into the phase stability and vibrational properties of the σ phase, which supported the completion of the last two papers. I would also like to extend my gratitude to the dedicated researchers at ICAMS, Ruhr-Universität Bochum –particularly Dr. Sergei Starikov, for his warm welcome and for introducing me to the art of potential fitting; Prof. Matous Mrovec; Prof. Ralf Drautz; and the entire team behind the ACE workshop.

Of course, I must thank my office mates –Praveen, Amin, Zhe, Peghar, and Elham– as well as my fellow Ph.D. students and colleagues, whose camaraderie made these years so rewarding. We have shared both challenges (Adams project!) and countless moments of laughter.

Finally, I am deeply thankful to my parents and my brother for their unwavering support throughout my life. To my love, Jiabao, thank you for always standing by me and for your patience during the demanding moments of my doctoral studies.

Popular summary in English

Fusion energy is one of the most exciting fields of research right now. In a world where global energy demands continue to rise and the negative impact of fossil fuels becomes increasingly evident, fusion energy promises to deliver an abundant source of clean energy without long-lived radioactive waste. The realization of fusion energy as a viable energy source is an incredible feat of engineering, requiring expertise in multiple scientific disciplines. The enormous scale of the task has given rise to the joke that "fusion energy is 30 years away – and always will be!" In reality, several breakthroughs toward fusion energy have been made in recent years, and records in plasma duration and energy output are being set at an increasing pace.

The components of a fusion reactor that face the plasma are referred to as plasma-facing components (PFCs). They are required to operate in an extreme environment characterized by high thermal loads, plasma exposure, and neutron irradiation. Finding the right materials for constructing PFCs is an exciting endeavor, as these materials must be able to withstand the harsh environment without negatively impacting plasma quality. Today, tungsten (W) is considered one of the most promising materials due to its high melting point, good thermal conductivity, and resistance to plasma exposure at low temperatures. For these reasons, W-based components are utilized in fusion reactors worldwide.

Despite the widespread implementation of W-based PFCs, there are also significant challenges with using W. Unlike most metals, W is brittle at moderate temperatures and has a high brittle-to-ductile transition temperature. The brittle fracture behavior limits the manufacturing and utilization of W-based components. Furthermore, the neutron irradiation is expected to cause further embrittlement of W. One of the unusual effects of irradiation is the transmutation of W into rhenium (Re) and osmium (Os), resulting in a change in the chemical composition of the component over time. Experiments have shown that Re and Os in irradiated W samples congregate and form incoherent precipitates of the type σ and χ. These precipitates are notorious for causing embrittlement in, e.g., stainless steels, and should be avoided to ensure the longevity of the reactor components. A deeper understanding of how these precipitates form and their impact on the mechanical properties of W is necessary to advance the development and implementation of W-based PFCs.

This study aims to investigate the σ and χ phases of W–Re and W–Os, illuminating the challenges they pose to W-based components. To this end, *ab initio* calculations have been employed to elucidate the intrinsic properties of

the phases, including their elastic properties, hardness, and fracture behavior. The phases are determined to be intrinsically hard and brittle. This is a concern, as brittle precipitates can initiate points of cracking, and hard, non-deformable precipitates can hinder dislocation motion, thereby increasing the brittleness of the material. Furthermore, a significant mismatch in the coefficient of thermal expansion (CTE) of the W–Re phases when compared to the surrounding W material was discovered. The mismatch grew with increasing temperature and Re content. For PFCs, which are expected to operate over a wide range of temperatures with cyclic thermal loading, the mismatch may pose a risk, as it can increase thermal stresses and the likelihood of crack initiation and thermal fatigue in the components. By investigating the mechanical and dynamic stability of the phases, it was discovered that the W–Os phase is mechanically unstable for high Os concentrations, and both the W–Re and W–Os σ phases were dynamically unstable for high Re and Os concentrations and may spontaneously transform into a new orthorhombic structure. This new knowledge is useful for determining the conditions under which the W–Re and W–Os σ phases will form. The results of this thesis provide insight into several intrinsic properties of the precipitates that form in neutron-irradiated W samples and may serve as a basis for further investigation into how they impact the durability and longevity of W-based PFCs.

Populärvetenskaplig sammanfattning på svenska

Fusionsenergi är ett av de mest spännande forskningsområdena just nu. I en värld där den globala energiefterfrågan fortsätter att öka och de negativa effekterna av fossila bränslen blir alltmer uppenbara, har fusionsenergi goda förutsätningar för att bli en riklig källa till ren energi utan långlivat radioaktivt avfall. Att göra fusionsenergi till en fungerande energikälla är en enastående ingenjörsbedrift som kräver expertis inom flera vetenskapliga discipliner. Den enorma omfattningen av uppgiften har gett upphov till skämtet att "fusionsenergi är 30 år bort – och kommer alltid att vara det!" I verkligheten har flera genombrott inom fusionsenergin gjorts de senaste åren, och nya rekord för både plasmalivslängd och energiutbyte slås i allt snabbare takt.

Komponenterna i en fusionsreaktor som är i direkt kontakt med plasman kallas plasmaexponerade komponenter (PFC:er). De måste fungera i en extrem miljö där de utsätts för höga termiska belastningar, plasmaexponering och neutronbestrålning. Att hitta de rätta materialen för att konstruera PFC:er är en spännande utmaning, eftersom dessa material måste kunna motstå den tuffa miljön utan att negativt påverka plasmans kvalitet. Idag anses volfram (W) vara ett av de mest lovande materialen för PFC:er, och W-baserade komponenter används i fusionsreaktorer världen över. Volfram anses lämpligt främst på grund av sin höga smältpunkt, goda termiska ledningsförmåga och motståndskraft mot plasmaexponering vid låga temperaturer.

Trots den utbredda användningen av W-baserade PFC:er finns det också betydande utmaningar med att använda W. Till skillnad från de flesta metaller är W sprött vid måttliga temperaturer och har en hög övergångstemperatur från sprött till duktilt tillstånd. Det spröda brottbeteendet begränsar både tillverkning och användning av W-baserade komponenter. Dessutom förväntas neutronbestrålning orsaka ytterligare sprödhet i W. En av de ovanliga effekterna av bestrålning är transmutation av W till rhenium (Re) och osmium (Os), vilket leder till en förändring av materialets kemiska sammansättning över tid. Experiment har visat att Re och Os ansamlas i bestrålade W-prover och bildar inkoherenta utfällningar av typen σ och χ. Dessa utfällningar är ökända för att orsaka sprödhet i exempelvis rostfria stål och bör undvikas. För att utvecklingen och implementeringen av W-baserade PFC:er ska kunna avancera, krävs en djupare förståelse för hur dessa utfällningar bildas och hur de påverkar W:s mekaniska egenskaper.

Denna studie syftar till att undersöka σ- och χ-faserna i W–Re och W–Os och belysa de utmaningar de medför för W-baserade komponenter. För detta

ändamål har *ab initio*-modellering använts för att klargöra fasernas mekaniska egenskaper, inklusive deras elastiska egenskaper, hårdhet och brottbeteende. Faserna har visat sig vara hårda och spröda. Detta är oroande, eftersom spröda utfällningar kan fungera som sprickinitieringspunkter och hårda utfällningar kan hindra dislokationsrörelse, vilket ytterligare ökar materialets sprödhet. Vidare upptäcktes en betydande avvikelse i den termiska expansionskoefficienten (CTE) hos W–Re-faserna jämfört med den omgivande W-matrisen. Skillnaden ökade med stigande temperatur och ökad Re koncentration. För PFC:er, som förväntas fungera över ett brett temperaturområde med cykliska termiska belastningar, kan denna skillnad utgöra en risk eftersom den kan bidra till ökade termiska spänningar och risken för sprickbildning i materialet. Genom att undersöka fasernas mekaniska och dynamiska stabilitet upptäcktes att W–Os-fasen är mekaniskt instabil vid höga Os-koncentrationer och att både W–Re och W–Osσ-faserna blir dynamiskt instabila vid höga Re- och Os-koncentrationer och kan spontant omvandlas till en ny ortorombisk struktur. Denna nya kunskap är användbar för att fastställa under vilka förhållanden W–Re och W–Os σ-faserna kommer att bildas. Resultaten från denna avhandling ger en inblick i flera hållfashets egenskaper hos de utfällningar som bildas i neutronbestrålade W-komponenter och bidrar till ökad förståelse för hur de påverkar hållfastheten och livslängden hos W-baserade PFC:er.

1 Introduction

1.1 Fusion energy

In a fusion power plant, energy is produced by fusing light elements into heavier ones. The fusion process that is deemed the most practical to pursue is the fusion of two hydrogen isotopes, deuterium ($^2_1$H) and tritium ($^3_1$H), into the helium isotope $^4_2$He and one neutron [1]

$$^2_1\mathrm{H} \ + \ ^3_1\mathrm{H} \ \longrightarrow \ ^4_2\mathrm{He} \ + \ ^1_0\mathrm{n} \ + \ 17.6 \text{ MeV} \tag{1}$$

The products on the right-hand side of the equation have slightly less mass than the combined mass of the two hydrogen isotopes. This phenomenon is called the mass defect, and the seemingly missing mass is converted into energy following Einstein's famous equation $E = mc^2$ [2, Chapter 4].

The produced energy is mainly in the form of heat and is utilized to drive a steam generator, similar to a conventional power plant. However, unlike a conventional fossil fuel or fission power plant, a fusion power plant can produce vast amounts of energy using only very little fuel and with no greenhouse gas emissions, atmospheric pollution, or long-lived radioactive waste[1]. Water and lithium, which are abundant, readily available, and relatively cheap, will be the raw fuels of a fusion power plant. Deuterium can be found in any water source, while tritium, which has a short half-life of 12.5 years, must be produced on-site. This can be achieved by bombarding lithium (Li) with neutrons produced as part of the fusion reaction (see Eq. (1)), thereby establishing a breeding cycle in which the fusion reactor produces the tritium it needs once the initial fusion process has started [2, Chapter 4]. It has been estimated that the lithium in a single laptop battery and a half bathtub of water can produce the same amount of energy as burning 40 metric tons of coal [2, Foreword].

For the fusion reaction in Eq. (1) to occur, the hydrogen gas must be heated up to more than 100 million degrees Celsius [2, Chapter 4]. At these temperatures, the hydrogen gas becomes a plasma in which the electrons are stripped from the nuclei. To keep the plasma from touching the walls of the fusion reactor, magnetic confinement can be used to keep the plasma suspended in the fusion chamber as the charged particles will follow the electromagnetic fields[2].

[1] Due to neutron irradiation from the fusion process the walls of the fusion reactor will contain some short-lived radioactive elements.

[2] An alternative way of confinement is inertial confinement in which a series of tiny fusion explosions are used to create energy.

Despite the magnetic confinement, any plasma-facing components (PFC) of the fusion reactor will be exposed to immense radiation heat up to 20 MW/m^2, resulting in temperatures between 600-1700°C depending on the reactor operation and the position of the component [3]. Design choices, such as active water cooling, also affect the temperature of the components. Additionally, due to edge-localized modes, in which the cooler outer layers of the plasma periodically expand, the PFCs may be directly exposed to the plasma and experience transient temperatures up to 2400°C [3]. In addition to the large temperatures and plasma exposure, the PFCs are also exposed to high-energy neutron irradiation, with neutron energies up to 14 MeV and penetration depths of up to several tens of centimeters [3]. This is because the neutrons produced as part of the fusion reaction in Eq. (1) do not have any electric charge and are not confined by the electromagnetic field. Neutron irradiation presents its own unique set of challenges, which will be covered in the next section of the thesis.

Plasma-facing components include the first-wall shielding, which protects the underlying structural materials, and the divertor, which functions as the reactor's "ashtray", letting out the heavier fusion products and potential impurities from the hydrogen plasma. The divertor, in particular, must withstand the harshest conditions in the reactor, as this component will be in direct contact with the plasma, causing high levels of sputtering and erosion [1]. Thus, selecting the right materials for the PFCs is a significant challenge that requires extensive research. Designing strong and durable PFCs is crucial to the longevity and usability of the fusion reactor.

1.2 Tungsten in plasma-facing components

Today, tungsten (W) is considered one of the most promising materials to use in PFCs [1, 5]. This is due to several advantageous properties such as a high thermal conductivity of around 150 W/mK at room temperature, a high melting point of 3680 K, and a low sputtering yield [3, 6].

The Joint European Torus (JET) project was one of the first fusion reactors to replace its old carbon-based components with W-based counterparts. Carbon-fiber composites were previously considered promising due to their high heat resistance and conductivity [5]. However, testing has proved that these components experienced significant chemical erosion due to exposure to the hydrogen plasma [5]. This raised concerns about tritium retention and the sputtering of C atoms into the plasma, thereby lowering plasma quality [1]. In comparison, W has an extremely low sputtering yield due to a high binding energy and, therefore, better resistance to plasma exposure [5, 7]. The modification of JET

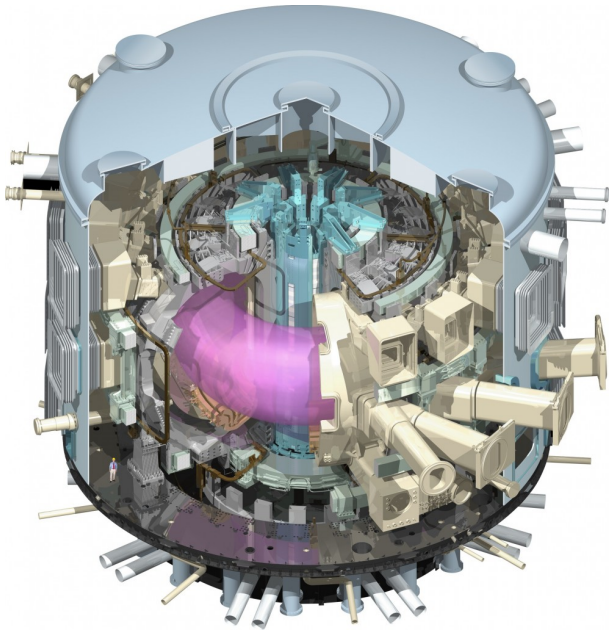

Figure 1: Artist's rendering of the ITER tokamak. The vacuum chamber has a torus shape. The hydrogen plasma is indicated with purple coloring. Powerful magnets surrounding the vacuum chamber produce the magnetic fields that confine the plasma. Reproduced with permission from [4].

proved to be a success with a reduction in tritium retention by an order of magnitude and a fivefold reduction of the rate of wall erosion [8, 9].

The successful testing of tungsten (W)-based components in JET has significantly influenced the design of other experimental reactors. For instance, in 2021, development began on a W-based divertor for the Wendelstein 7-X reactor, with the long-term goal of creating a carbon-free plasma-facing environment using W-based PFCs [10]. The experimentation done on JET directly informs the design choices of the International Thermonuclear Experimental Reactor (ITER) currently under construction in southern France. A schematic of the reactor is shown in Figure 1. ITER is arguably the most important test reactor for demonstrating the feasibility of fusion as a viable energy source [11]. It will be the biggest Tokamak-type reactor in the world and will feature a W-based divertor [12]. Plans for the next fusion reactor plant, called DEMO, are currently being developed, where W-based PFCs are expected to play a crucial role in its design [3].

The biggest challenge for W-based PFCs is the brittleness of W. Compared to

other metals, W has an unusually high brittle-to-ductile transition temperature. It is known to exhibit brittle fracture behavior up to temperatures of approximately 600 K, which is part of the required operational temperatures for PFCs with active water cooling [6]. Furthermore, neutron irradiation has been shown to increase the brittle-to-ductile transition temperature by up to an additional 500 K [13].

Neutron irradiation affects the brittle-to-ductile transition temperature and mechanical properties of W by causing several types of irradiation damage, such as dislocations, voids, interstitials, and precipitation [14]. One of the more exotic effects of neutron irradiation is the transmutation of W into its transmutation products Re and Os, meaning that the chemical composition of the component will change during the operating lifetime. It is predicted that the composition after 5 years of service will be approximately 91 at.% W, 6 at.% Re and 3 at.% Os in the first wall armor in an ITER-like reactor [15]. Under equilibrium conditions, the addition of small amounts of Re to W may improve the ductility [16], however, in the environment of a fusion reactor, nonequilibrium radiation-induced precipitation mechanisms cause the Re and Os to congregate and form two types of incoherent precipitates known as σ and χ [15, 17]. These precipitates have been shown to form even when the transmutation product concentration is just a few percent [18–22], which is within the expected transmutation concentration of W-based PFCs while in operation [15, 23].

The σ and χ precipitates raise concerns, as they are known to embrittle the host material [24, 25]. The phases belong to a group of topologically close-packed phases that form in transition metal alloys such as W–Re and W–Os. The σ phase has tetragonal crystal symmetry and belongs to the space group $P4_2/mnm$. The unit cell, shown in Figure 2(a), contains 30 atoms located on the following five nonequivalent lattice sites, known as Wyckoff sites: $2a$, $4f$, $8i_1$, $8i_2$, and $8j$. The number refers to the multiplicity of the site, while the letter refers to the Wyckoff position. The coordination numbers of the sites are, respectively, 12, 15, 14, 12, and 14. The χ phase has a cubic crystal symmetry belonging to the $I\bar{4}3m$ space group. The cubic unit cell, shown in Figure 2(b), comprises 58 atoms distributed among the four Wyckoff sites: $2a$, $8c$, $24g_1$, and $24g_2$ with the following coordination numbers: 16, 16, 13, and 12, respectively. The phases are known not to have a fixed stoichiometry and can be stable for a wide range of concentrations at elevated temperatures. Despite this, complete random disorder is not observed either as studies indicate that elements with more than half-filled d-orbitals, such as Re and Os, prefer the low coordination number sites [26, 27]. Under equilibrium conditions, the W–Re σ phase becomes thermodynamically stable in the concentration range 44-62 at.% Re, while the

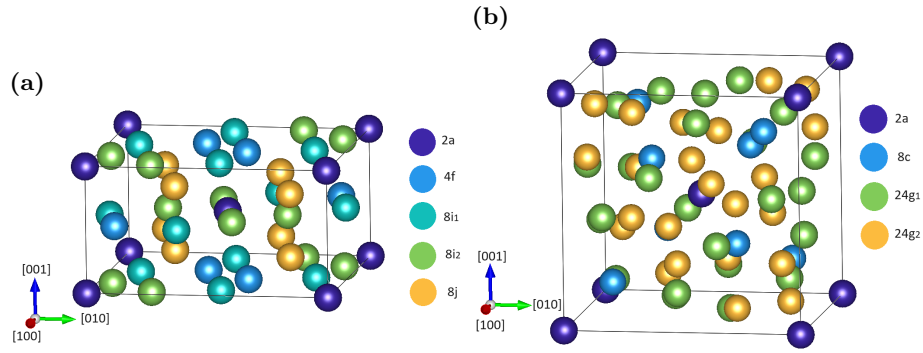

Figure 2: The standard unit cells of (a) the σ and (b) χ phase visualized using VESTA [29]. The unique lattice sites, known as Wyckoff sites, have been color-coded.

W–Re χ phase is stable at higher Re contents in a narrow range of 72-74 at.% Re [28]. For the W–Os system the σ phase is stable for Os contents in the range of 20-35 at.% Os, while the χ phase has not been reported to be stable [28].

As W is already a very brittle material, the presence of σ and χ precipitates is cause for concern, as they may affect the longevity and durability of the W-based PFCs. It may also limit the use of W in structural components as a brittle failure of these would be severe. Understanding how the formation of σ and χ precipitates affects the mechanical properties of W is crucial for assessing the usability of W-based PFCs. It can also help inform the design choices for the next generation of W-based PFCs in fusion reactors.

1.3 Objectives of this work

The objectives of this thesis work are to study the properties of the σ and χ phases in W–Re and W–Os in order to assess the challenges they impose on W-based components. To this end, *ab initio* calculations are used to unveil the intrinsic properties of the phases, such as the elastic properties, thermal expansion, stability, and fracture behavior. As experimental data on the mechanical and thermodynamic properties of the phases are currently lacking, computational methods can provide valuable insights. It also provides the advantage of obtaining the aforementioned properties as a function of the Re and Os concentration, thereby investigating how the chemical composition affects the properties of the phases. This is important for the σ and χ phases as they do not have a fixed stoichiometry but are thermodynamically stable for a wide range of temperatures.

The following three research objectives of this thesis have been formulated:

- Investigate the formation, structure, and stability of the σ and χ phases in W–Re and W–Os for varying stoichiometry.
- Evaluate the mechanical and fracture-related properties of the σ and χ phases as a function of the Re and Os content.
- Determine the volumetric thermal expansion of the precipitates and quantify the mismatch with the surrounding W-matrix.

2 First-principles methods

In this section, the fundamentals of first-principle methods used to obtain the results of this thesis work will be introduced.

2.1 The many-body Schrödinger equation

From a quantum mechanical perspective, a solid consists of electrons and nuclei. To describe the system quantum mechanically, the Schrödinger equation of the system is written as

$$\hat{H}\Psi = E\Psi \tag{2}$$

where $\hat{H}$ is the Hamiltonian, Ψ is the many-body wavefunction and E is the energy of the state described by Ψ. In the following, bold font, e.g., $\mathbf{r_i}$, represents vectors, and Hartree atomic units are employed consistently. The many-body wavefunction depends on the positions of the electrons and the nuclei. Let there by N electrons with coordinates $\mathbf{r}_1, \mathbf{r}_2, ..., \mathbf{r}_N$ and M nuclei with coordinates $\mathbf{R}_1, \mathbf{R}_2, ..., \mathbf{R}_M$ in the solid:

$$\Psi = \Psi\left(\mathbf{r}_1, \mathbf{r}_2, ..., \mathbf{r}_N; \mathbf{R}_1, \mathbf{R}_2, ..., \mathbf{R}_M\right) \tag{3}$$

The Hamiltonian consists of the kinetic and potential energy of the system: $\hat{H} = \hat{T} + \hat{V}$. The kinetic energy is written as

$$\hat{T} = -\sum_{i=1}^{N} \frac{\nabla_i^2}{2} - \sum_{I=1}^{M} \frac{\nabla_I^2}{2M_I}, \tag{4}$$

where M_I is the mass of the nuclei and ∇^2 is the Laplace operator. The potential energy of the system is given by the Coulomb interaction between electrons and nuclei

$$\hat{V} = \frac{1}{2}\sum_{i\neq j}\frac{1}{\mathbf{r}_i - \mathbf{r}_j} + \frac{1}{2}\sum_{I\neq J}\frac{Z_I Z_J}{\mathbf{R}_I - \mathbf{R}_J} - \sum_{i,I}\frac{Z_I}{\mathbf{r}_i - \mathbf{R}_J}, \tag{5}$$

where Z_I and Z_J are the atomic number and the indices i and j run from 1 to N while indices I and J run from 1 to M.

The massive difference in mass between electrons and nuclei has not been taken into consideration so far. For reference, the mass of an electron is roughly 1800 times less than a proton[3]. This means that the electrons can be assumed to have found their ground state in the time frame of the nuclei moving [30, Chapter 4], or, differently put, the nuclei are practically immobile on the timescale of the electrons [31, Chapter 2]. This is known as the Born-Oppenheimer approximation. When applied, the kinetic energy term of the nuclei in Eq. (4) becomes negligible ($M_J = \infty$) and, if the positions of the nuclei are known e.g. in a crystal lattice, the Coulomb interaction between the nuclei becomes a constant term that can be absorbed into the energy E. The many-body equation can therefore, be rewritten as

$$\left[-\sum_{i=1}^{N}\frac{\nabla_i^2}{2} + \sum_i \hat{V}_n(\mathbf{r}_i) + \frac{1}{2}\sum_{i\neq j}\frac{1}{\mathbf{r}_i - \mathbf{r}_j}\right]\Psi = E\Psi, \tag{6}$$

where the many-body wavefunction, $\Psi(\mathbf{r}_1, \mathbf{r}_2, ..., \mathbf{r}_N)$, depends on the electron positions only, and $\hat{V}_n$ is the electron-nuclei Coulomb interaction:

$$\hat{V}_n(\mathbf{r}_i) = -\sum_I \frac{Z_I}{\mathbf{r}_i - \mathbf{R}_J}. \tag{7}$$

Despite the simplicity of Eq. (6), the Coulomb interaction between the electrons becomes prohibitively expensive to compute for any real solid. The mean-field approximation provides a method for estimating the Coulomb interaction in a solvable manner. In the mean-field approximation, the electrons are assumed to be non-interacting. That is, the interaction many-body wavefunction can be written as the product function of single-particle wavefunctions, $\phi_i(\mathbf{r}_i)$:

$$\Psi(\mathbf{r}_1, \mathbf{r}_2, ..., \mathbf{r}_N) = \prod_{i=1}^{N}\phi_i(\mathbf{r}_i) \tag{8}$$

[3]The nuclei consist of several protons and neutrons, which have approximately the same mass. The mass difference between neutrons and protons is around 0.1%.

The electron density, $\rho(\mathbf{r}) = \sum_i |\phi_i(\mathbf{r})|^2$, gives rise to an electrostatic potential, $\varphi(\mathbf{r})$, according to Poisson's equation: $\nabla^2\varphi(\mathbf{r}) = 4\pi\rho(\mathbf{r})$. By introducing the Hartree potential as $\hat{V}_H(\mathbf{r}) = -\varphi(\mathbf{r})$ and solving the Poisson's equation, the following expression is obtained:

$$\hat{V}_H(\mathbf{r}) = \int \mathrm{d}\mathbf{r}' \frac{\rho(\mathbf{r}')}{|\mathbf{r} - \mathbf{r}'|} \tag{9}$$

Instead of interacting with each other directly, the electrons interact with the electron mean-field produced by the independent electrons. The $\phi_i(\mathbf{r_i})$ are then obtained by solving the non-interacting single-electron Schrödinger equation:

$$\left[-\frac{\nabla^2}{2} + \hat{V}_n(\mathbf{r}) + \hat{V}_H(\mathbf{r})\right] \phi_i(\mathbf{r}) = \varepsilon_i \phi_i(\mathbf{r}) \tag{10}$$

where the eigenvalue ε_i is the energy of the single-particle ϕ_i state.

While the mean-field approximation allows for the problem to be solved, it leaves out two important aspects of the electron interaction. Firstly, the electronic wavefunctions must fulfill Pauli's exclusion principle, which states that two electrons cannot occupy the same state [32]. This implies that the many-body wavefunction Ψ must change sign if the variables of two electrons are exchanged, something that Eq. (8) does not guarantee in general [31, Chapter 2]. Secondly, the correlation between electrons has not been considered. Due to the repulsive Coulomb interaction between electrons, an electron is less likely to be situated in close proximity to another electron [31, Chapter 2]. In the following section, the Density Functional Theory (DFT) method developed by Hohenberg, Kohn, and Sham [33, 34] will be introduced as it offers a clever solution to these issues.

2.2 Density Functional Theory

The Hohenberg-Kohn theorem [33] states that the *ground state energy* is a functional of the electron density only: $E = \mathcal{F}[\rho]$. The proof of the theorem is based on two key principles. First, two distinct external potentials cannot produce the same ground state. Second, the ground state represents the lowest possible energy for the system. The ground state density, denoted as ρ_0, is precisely the density that minimizes the energy, i.e.: $\frac{\delta\mathcal{F}[\rho]}{\delta\rho}\Big|_{\rho_0} = 0$ [31, Chapter 3].

The idea of Kohn and Sham [34] was to write the ground state energy functional using the independent electrons plus an additional functional term, $E_{xc}[\rho]$, that accounts for the difference in energy between the real many-body system (where

electrons are subjected to the Pauli rule of exchange and correlation) and the simplified independent electron system. If the wavefunctions are required to be orthonormal and the Hohenberg-Kohn variational principle is applied, it leads to the following equation, called the Kohn-Sham equation: [31, Chapter 3]

$$\left[-\frac{\nabla^2}{2} + \hat{V}_n(\mathbf{r}) + \hat{V}_H(\mathbf{r}) + \hat{V}_{xc}(\mathbf{r})\right]\phi_i(\mathbf{r}_i) = E\phi_i(\mathbf{r}_i) \tag{11}$$

where $\hat{V}_{xc}(\mathbf{r}) = \frac{\delta E_{xc}[\rho]}{\delta\rho}\Big|_{\rho(\mathbf{r})}$ is the exchange and correlation potential. The electron density is obtained by summation over the spatial probability of the occupied single electron wavefunctions:

$$\rho(r) = \sum |\phi(\mathbf{r})|^2. \tag{12}$$

The ingenuity of the Kohn-Sham theory is that if the exact E_{xc} is known, all many-body effects are, in principle, included in Eq. (11) [35]. This is, however, not the case, and the success of DFT relies on accurate and computationally efficient approximations of E_{xc}, of which multiple have been constructed over the years. In this thesis work, the commonly applied generalized gradient approximation (GGA) has been used.

$$E_{xc}^{GGA} = \int \mathrm{d}\mathbf{r}\rho(\mathbf{r})\epsilon_{xc}^{GGA}\left(\rho(\mathbf{r})|\nabla\rho(\mathbf{r})\right) \tag{13}$$

where the $\epsilon_{xc}^{GGA}\left(\rho(\mathbf{r})|\nabla\rho(\mathbf{r})\right)$ is the exchange-correlation energy per electron that depends on the density $\rho(\mathbf{r})$ and the gradient $\nabla\rho(\mathbf{r})$. The ground-state energy of the system is obtained through a self-consistency loop, using an initial guess for the electron density. The process of the DFT algorithm is illustrated in Figure 3.

The electron wavefunction of a real material behaves differently in different regions of space [37]. In the chemical bonding region, located far away from the nuclei, the wavefunction behaves smoothly, and a set of plane waves is an appropriate choice for $\phi_i(\mathbf{r})$. For the core region, however, the strong Coulomb interaction with the nuclei at short distances causes the wavefunctions to exhibit rapid oscillations [37]. To accurately model the core behavior would require an impractically large set of plane waves, and a set of atomic orbital-like functions is the preferred choice. To work around this dilemma, the projector augmented wave (PAW) method developed by Blöchl [37] was employed. The general approach of augmented-wave methods is to divide the wavefunction into regions: in localized regions close to the nucleus the wavefunction is evaluated using atomic orbital-like functions. Outside the regions, the smooth part of the wavefunction

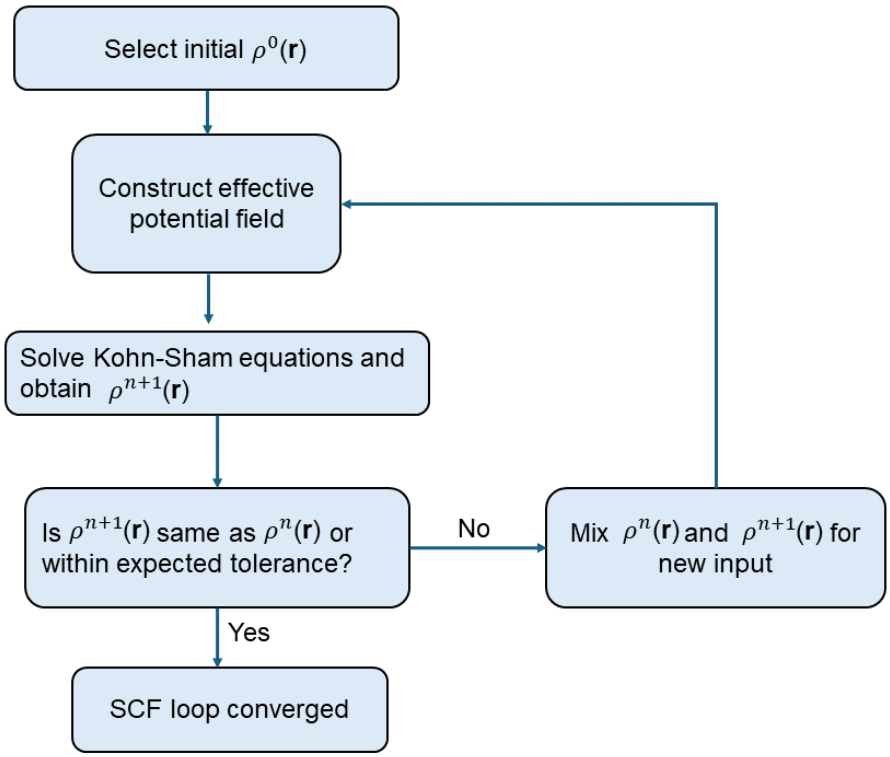

Figure 3: Flow chart of the DFT framework. Adopted with permission from [36].

is evaluated using plane waves [38, Chapter 11]. The PAW method uses projector functions to match the two regions [37]. It has proven to be efficient and accurate, especially for transition metals, where the method has shown to reduce errors in energy calculations compared to other commonly used pseudopotential methods [39].

2.3 Vibrational properties of solids

Vibrations within the crystal lattice, referred to as phonon modes, play a crucial role in influencing the crystal's free energy, thermodynamic stability, and various physical properties, including thermal expansion and elastic moduli [40]. Additionally, evaluating the phonon band structure and the phonon density of states (PDOS) is essential for assessing the dynamic stability of the crystal [40]. To describe the free energy and coefficient of thermal expansion of the σ and χ phases, the harmonic and quasi-harmonic approximation were utilized.

2.3.1 The Harmonic Approximation

The potential energy of a crystal structure with nuclei displaced from their equilibrium positions can be written as a Taylor expansion [31, Chapter 7]:

$$U = U_0 + \Phi_I^\alpha u_I^\alpha + \frac{1}{2}\Phi_{IJ}^{\alpha\beta} u_I^\alpha u_J^\beta + \frac{1}{3!}\Phi_{IJK}^{\alpha\beta\gamma} u_I^\alpha u_J^\beta u_K^\gamma + \mathcal{O}(\mathbf{R}^4) \tag{14}$$

where U_0 is the energy of the non-displaced system, Φ are the force constants, nuclei are indicated with Latin letters I, J, K, and cartesian coordinates with Greek letters α, β, γ. The Einstein summation convention has been applied to shorten the expression. The displacement of a nucleus I from its equilibrium position $\mathbf{R_0}$ is indicated by $u_I^\alpha = R_I^\alpha - R_{I,0}^\alpha$. To predict the vibrational behavior, the force constants of the material must be determined. The force constants are independent of time as they are evaluated at the nuclei's equilibrium position. At the equilibrium position, the force on each nuclei is zero, meaning that the linear term in Eq (14) vanishes. The second-order force constants are defined as [41]

$$\Phi_{IJ}^{\alpha\beta} = \left.\frac{\partial^2 U}{\partial R_I^\alpha \partial R_J^\beta}\right|_{\mathbf{R}=\mathbf{R_0}}. \tag{15}$$

In the harmonic approximation, only force constants up to the second order are considered, meaning that the energy of the vibrating crystal lattice can be approximated as

$$U = U_0 + \frac{1}{2}\Phi_{IJ}^{\alpha\beta} u_I^\alpha u_J^\beta. \tag{16}$$

The second-order force constants can be obtained using the direct method, also known as the finite difference method. This method provides reliable results and has been implemented in several software packages, such as Phonopy [42, 43], which was utilized in this thesis work. The nuclei are displaced in each independent direction, and the forces on the nuclei are computed using DFT. The second-order force constants are obtained via numerical fitting of the forces and displacements [42, 43]. The number of unique force constants can be greatly reduced when exploiting the symmetry of the crystal lattice.

Once the force constants are known, the dynamical properties of the crystal, such as the phonon modes, are determined by constructing the dynamical matrix $D(\mathbf{q})$ for a reciprocal wave vector $\mathbf{q}$. The elements of the dynamical matrix are

$$D_{I,J}^{\alpha\beta}(\mathbf{q}) = \frac{1}{\sqrt{M_I M_J}} e^{-i\mathbf{q}\cdot(\mathbf{R_J}-\mathbf{R_I})} \Phi_{I,J}^{\alpha\beta}. \tag{17}$$

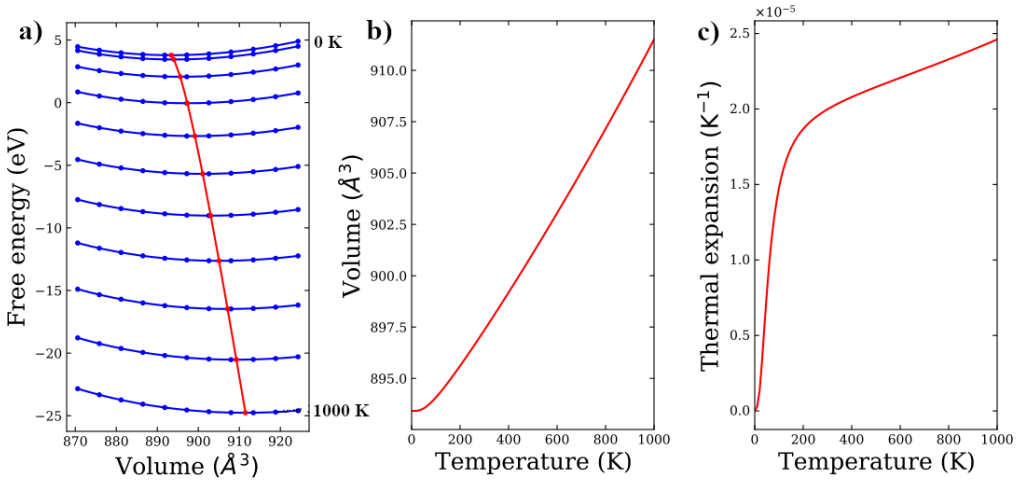

Figure 4: The process of computing the coefficient of thermal expansion (CTE), taking the χ phase as an example.

The harmonic frequencies are obtained by solving the eigenvalue problem

$$D^{\alpha\beta}_{I,J}(\mathbf{q})e^{\beta}_{J,\nu}(\mathbf{q}) = \omega^2_{\nu}(\mathbf{q})e^{\alpha}_{I,\nu}(\mathbf{q}), \tag{18}$$

where $\omega_{\nu}(\mathbf{q})$ is the harmonic frequency at the wavevector $\mathbf{q}$ with mode index ν and $e^{\alpha}_{I,\nu}(\mathbf{q})$ is the corresponding eigenvector. The PDOS, $g(\omega)$, is calculated from $\omega_{\nu}(\mathbf{q})$, i.e.

$$g(\omega) = \sum_{\nu} \int \frac{d\mathbf{q}}{(2\pi)^3} \delta\left(\omega - \omega_{\nu}(\mathbf{q})\right). \tag{19}$$

2.3.2 The Quasi-Harmonic Approximation

When materials are heated, they tend to undergo thermal expansion. When the volume is increased, the phonon frequencies tend to soften, resulting in weakened elastic properties and reduced bond strength. The behavior of thermal expansion can be modeled using the quasi-harmonic approximation (QHA), in which the harmonic approximation is applied to a series of expanded and compressed volumes around the equilibrium volume. The process is visualized for the χ phase in Figure 4. For each volume, the Helmholtz free energy is computed and fitted to the Birch-Munaghan equation of state [44], as shown in Figure 4(a). This allows for the free energy to be estimated as a function of temperature and volume: $F(T, V)$. The equilibrium volume, at zero external pressure, is then

found as a function of temperature by finding the volume that minimizes the free energy at a given temperature:

$$V_{eq}(T) = \arg\min_{V} \left[F(T,V)\right], \tag{20}$$

as shown in Figure 4(b). Finally, the volumetric coefficient of thermal expansion (CTE) as a function of temperature is then obtained by numeric differentiation of the $V_{eq}(T)$ as shown in Figure 4(c).

The Helmholtz free energy can be expressed as:

$$F(T,V) = E_0(V) + F_{el}(T,V) + F_{vib}(T,V) \tag{21}$$

where E_0 is the strain energy, F_{el} is the contribution due to electronic excitations[4] and F_{vib} is the vibrational free energy. In the QHA, the vibrational free energy is calculated directly from the PDOS, i.e.

$$\begin{aligned} F_{vib}^{QHA}(T,V) = &\frac{1}{2}\int_0^\infty g(\omega,V)\,\hbar\omega d\omega + ... \\ &k_B T \int_0^\infty g(\omega,V) \ln\left[1 - \exp\left(-\frac{\hbar\omega}{k_B T}\right)\right] d\omega, \end{aligned} \tag{22}$$

where ω is the phonon frequency, $\hbar$ is the reduced Planck constant, k_B is the Boltzman constant, and $g(\omega, V)$ is the PDOS at a volume V [45].

2.3.3 The Debye-Grüneisen model

While the QHA gives very accurate results, it is also computationally expensive, especially for large structures such as the σ and χ phases. In the acoustic-based Debye-Grüneisen (DG) model, the optical phonon modes are approximated as acoustic ones, thereby significantly reducing computational costs. Since the vibrational free energy relies on the integration of the PDOS, making it less sensitive to the specific structure of the PDOS, the DG model can often yield accurate results despite its simplification [46].

Within the DG model, the vibrational free energy is estimated as [47]:

$$F_{vib}^{DG}(T,V) = -nk_BT\left[3\left(\frac{T}{\Theta}\right)^3 \int_0^{\Theta/T} \frac{x^3}{e^x - 1} dx - 3\ln\left(1 - e^{-\frac{\Theta}{T}}\right) - \frac{9\Theta}{8T}\right] \tag{23}$$

[4]The expression of the electronic term is omitted here due to its complexity, but it is provided in Paper II.

with n being the number of atoms in the unit cell, $x = \frac{\hbar\omega}{k_B T}$, and Θ is the Debye temperature which relates to the highest occupied frequency, ω_m, called the "cut-off" frequency: $\Theta = \frac{\hbar\omega_m}{k_B}$. The volume dependency of Θ is approximated by utilizing the expression introduced by Moruzzi et al. [48], that is

$$\Theta\left(V, V_0\right) = \Theta_0 \left[\frac{V_0}{V}\right]^{\gamma}, \tag{24}$$

where the Debye temperature evaluated at the equilibrium volume, Θ_0, can be estimated using the elastic constants of the structures [49], and γ is the Grüneisen parameter. The Grüneisen parameter describes how the vibrational properties change with volume and is therefore an indicator of the anharmonicity of the lattice vibrations [50]. The result of the DG model is highly sensitive to the choice of calculating γ. In this work the commonly-used Slater approximation [51] is utilized, in which γ is estimated as

$$\gamma = -\frac{2}{3} - \frac{V}{2}\frac{\partial^2 P/\partial V^2}{\partial P/\partial V}, \tag{25}$$

where P is the static lattice pressure at 0 K [49]. As a first approximation, γ can be assumed to be volume-independent, meaning that Eq. (25) is evaluated at the equilibrium volume V_0 [48]. After calculating the vibrational free energy over a range of volumes around V_0, the Helmholtz free energy (see Eq.(21)) is fitted to the Birch-Murnaghan equation of state, and the CTE is then determined numerically as described in the previous section.

2.4 Fracture mechanisms at atomic scale

The presence of defects, such as microscopic cracks, promotes the failure of a material in the form of fracture. According to Griffith's and Rice's theories of fracture, the event occurring at the crack tip is a competition between brittle and ductile fracture mechanisms [52, Chapter 2]. The crack can either grow through brittle fracture along the crack plane, or the crack tip can blunt through dislocation emission along a slip plane [52, Chapter 2]. In Figure 5, a schematic of such a crack system is shown. In the following, mode-I loading of the crack is assumed, in which uniaxial loading perpendicular to the crack faces is applied. According to Rice's theory of fracture [53], the criterion for crack tip blunting before brittle fracture under mode I loading is

$$D \equiv \frac{G_I^{klm}}{2\gamma_{us}^{k'l'm'}} > 4\frac{1 + (1-\nu)\tan^2\phi}{(1+\cos\theta)\sin^2\theta} \tag{26}$$

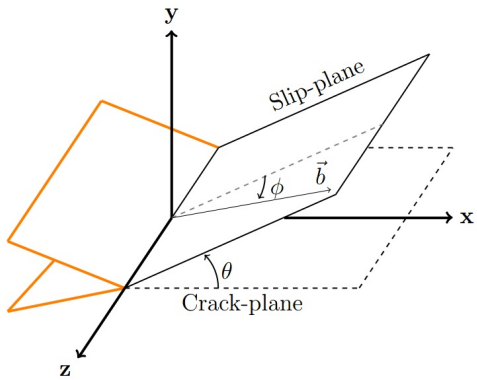

Figure 5: Crack plane and slip system with slip direction **b** defined by angles θ and ϕ.

where the angles θ and ϕ are defined the Figure 5 and ν is the Poisson ratio. The parameter G_I^{klm} is the energy release rate associated with the formation of two new surfaces. For ideal brittle fracture, it is estimated as $G_I = 2\gamma_s^{klm}$, where γ_s^{klm} is the surface energy of the newly created surface with Miller indices (klm). The unstable stacking fault energy, $\gamma_{us}^{k'l'm'}$, can be viewed as the energy barrier for slip along a plane with Miller indices $(k'l'm')$.

Brittle and ductile mechanisms tend to occur on the close-packed planes of the crystal. The close-packed planes of the σ and χ phases were determined using the structure factor as described in [54]. The planes relevant for fracture in σ and χ were determined to be the {330} and {004} planes, respectively, based on their close-packing of atoms and their low values of G_I and $\gamma_{us}^{k'l'm'}$ [55]. The generalized stacking fault energy surfaces of the relevant close-packed planes of the W–Re σ phase are shown in Figure 6(a) and (c). In the figure, different shearing paths are showcased, and the resulting stacking fault energies are plotted in (b) and (d). The paths drawn with black dashed lines are preferred for slip as they result in the lowest energy barriers. The identified slip systems are $\{330\}\langle 001\rangle$ and $\{004\}\langle 100\rangle$ and the height of these curves is the $\gamma_{us}^{k'l'm'}$. Experimental studies on the Fe–Cr σ phase [56, 57] identified two additional slip systems, which were investigated for W–Os in Paper III. They are omitted from this work for brevity, as they were found to yield higher values of $\gamma_{us}^{k'l'm'}$ and exhibited the same concentration-dependent trends.

By limiting the analysis to the {004} and {330} close-packed planes, the criterion in Eq. (26) becomes:

$$D^{004} \equiv \frac{G_I^{004}}{2 \cdot \gamma_{us}^{330}} > 4 \tag{27}$$

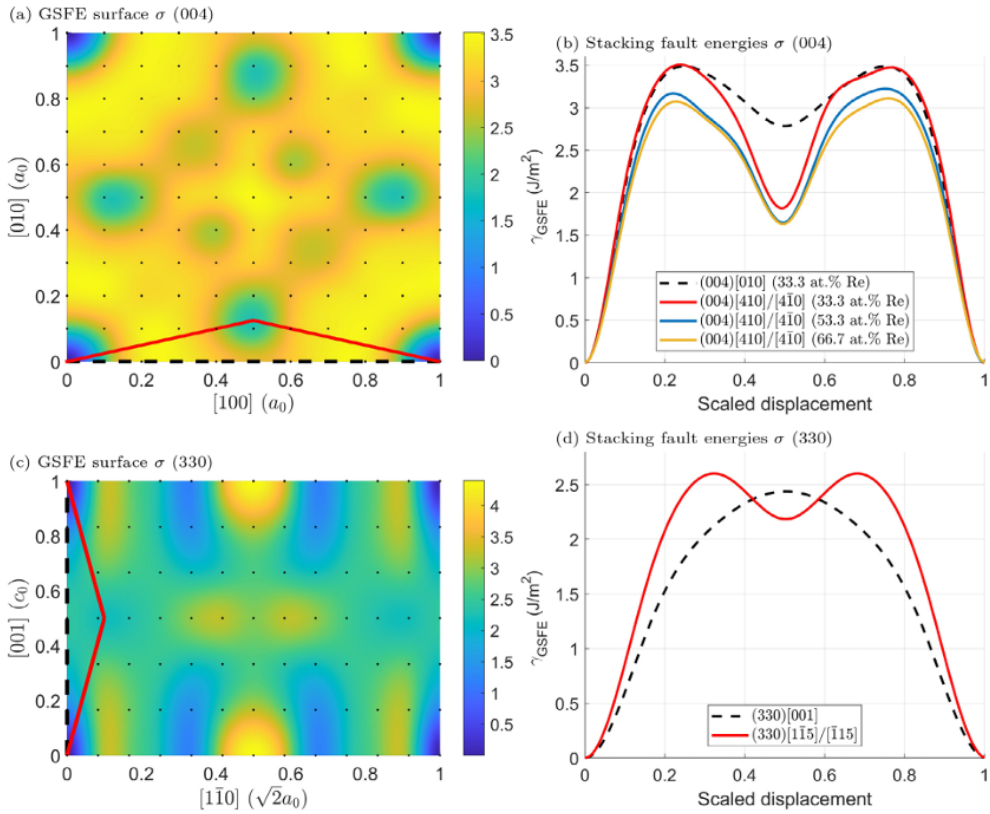

Figure 6: Left column (a) and (c): GSFE surfaces of the close-packed planes of the σ-phase. Black dots are DFT data points, a 2D spline-fit is used for interpolation. The colored lines indicate possible low-barrier paths for shearing. Right column (b) and (d): The stacking fault energies of the shearing paths are shown.

for the {004} crack plane, and for the {330} crack plane

$$D^{330} \equiv \frac{G_I^{330}}{2 \cdot \gamma_{us}^{004}} > 4 \cdot (2 - \nu). \tag{28}$$

The parameters D^{004} and D^{330} will be referred to as the ductility parameters of the crack planes. It should be noted that in this simplistic view, crack tip behavior such as lattice trapping [58], which may increase the resistance to brittle fracture, and other types of ductile mechanisms, e.g. twinning, have not been considered.

2.5 The Sublattice Model

Although the σ and χ phases are non-stoichiometric, complete disorder of the lattice site position of the elements is not observed [59]. To capture the disorder in the σ and χ phases and to determine the preferred lattice site occupancy of the elements, the sublattice model has proven successful [26, 27, 60]. In this model, the Wyckoff sites of the crystal phase are treated as sublattices occupied by a single element [60]. For the σ phase, which has five Wyckoff sites, this means $2^5 = 32$ unique configurations, while for the χ phase, which has four Wyckoff sites, there are $2^4 = 16$ configurations.

In the following, the method will be explained briefly, taking the W–Re σ as an example. The process is identical for a W–Os σ phase (just by replacing Re with Os) and the W–Re χ phase (bearing in mind the difference in the number of Wyckoff sites). The ground state energy per atom of the unique σ configurations is denoted as E^{klmno}, with the indices k, l, m, n, and o referring to the occupation of the, respectively, $2a$, $4f$, $8i_1$, $8i_2$, and $8j$ Wyckoff sites.

The formation enthalpy, H_f, at 0 K of the configuration was computed by subtracting the energies of W and Re in their reference states, i.e., body-centered cubic (BCC) W and hexagonal close-packed (HCP) Re,

$$H_f^{klmno} = E^{klmno} - x_W \cdot E_W^{BCC} - x_{Re} \cdot E_{Re}^{HCP}, \tag{29}$$

where x_c is the concentration of element c in the $klmno$ configuration and the reference state energies are E_W^{BCC} and E_{Re}^{HCP}.

Under the assumption of ideal mixing on the sublattice sites, Gibbs free energy of a disordered σ phase with Re concentration x_{Re} at a temperature T, can thereby be written as [61].

$$G(x_{Re}, T) = H^{ref}(x_{Re}) - T \cdot S^{mix}(x_{Re}). \tag{30}$$

The first term in Eq. (30) is a site-occupancy-weighted sum of the H_f^{klmno} of all the possible sublattice configurations of the σ phase [27]

$$H^{ref}(x_{Re}) = \sum_{k,l,m,n,o=W,Re} \left(y_k^{2a} y_l^{4f} y_m^{8i_1} y_n^{8i_2} y_o^{8j} \right) \cdot H_f^{klmno} \tag{31}$$

where y_c^s is the atomic fractions of element c on Wyckoff site s. For a binary system, it follows that for a given Wyckoff site s: $y_W^s + y_{Re}^s = 1$. While not written explicitly for the sake of clarity, the Wyckoff site occupations depend on the temperature and the transmutation product concentration: $y_k^s(x_{Re}, T)$.

The second term in Eq. (30), contains the configurational entropy of ideal mixing on the sublattices is:

$$S^{mix}(x_{Re}) = \frac{k_B}{N_{cell}} \sum_s m_s \sum_{k=W,Re} y_c^s \ln y_k^s. \tag{32}$$

where k_B is Boltzmann's constant, N_{cell} number of atoms in the σ unit cell and m_s is the multiplicity of Wyckoff site s. By minimizing Eq. (30) with respect to y_k^s at a fixed temperature, the preferential y_k^s were determined as a function of x_{Re}. The temperature of 1500 K was chosen since it has been shown to give well-matched results with experiments for the W–Re σ phase [26].

Just as the formation enthalpy was expressed in a sublattice model in Eq. (31), the same can be done for other properties of the phase [62]. For example, the bulk modulus, K_V, of a disordered σ phase with Re content x_{Re} are within this approximation given as:

$$K_V(x_{Re}) = \sum_{k,l,m,n,o=W,Re} \left(y_k^{2a} y_l^{4f} y_m^{8i_1} y_n^{8i_2} y_o^{8j} \right) \cdot K_V^{klmno} \tag{33}$$

where K_V^{klmno} is the bulk moduli of the sublattice configurations and the y_k^s are the preferential atomic fractions. In this sense, $K_V(x_{Re})$ can be seen as a weighted average of the sublattices using the y_k^s's as weights.

3 Results and Discussion

In the following sections, the major results of the papers included in this thesis work are compiled and summarized. The results has been divided into four sections. Section 3.1 deals with the structure and stability of the phases and compiles results from Papers I, III, and IV. In the following section 3.2, the results of the studies on mechanical and fracture-related properties, based on Papers I and III, are presented. In section 3.3, the dynamic stability and phase transformations of the σ are presented based on the results of Paper IV. Finally, in section 3.4, the results on the thermal expansion of the W–Re σ and χ phases are presented based on the findings of Paper II.

3.1 Structure and stability

To understand the formation of the σ and χ phases in W–Re and W–Os alloys, knowledge of their stability and structure is needed. In this section, the sublattice model is applied to calculate the formation enthalpy, H_f, of the phases and

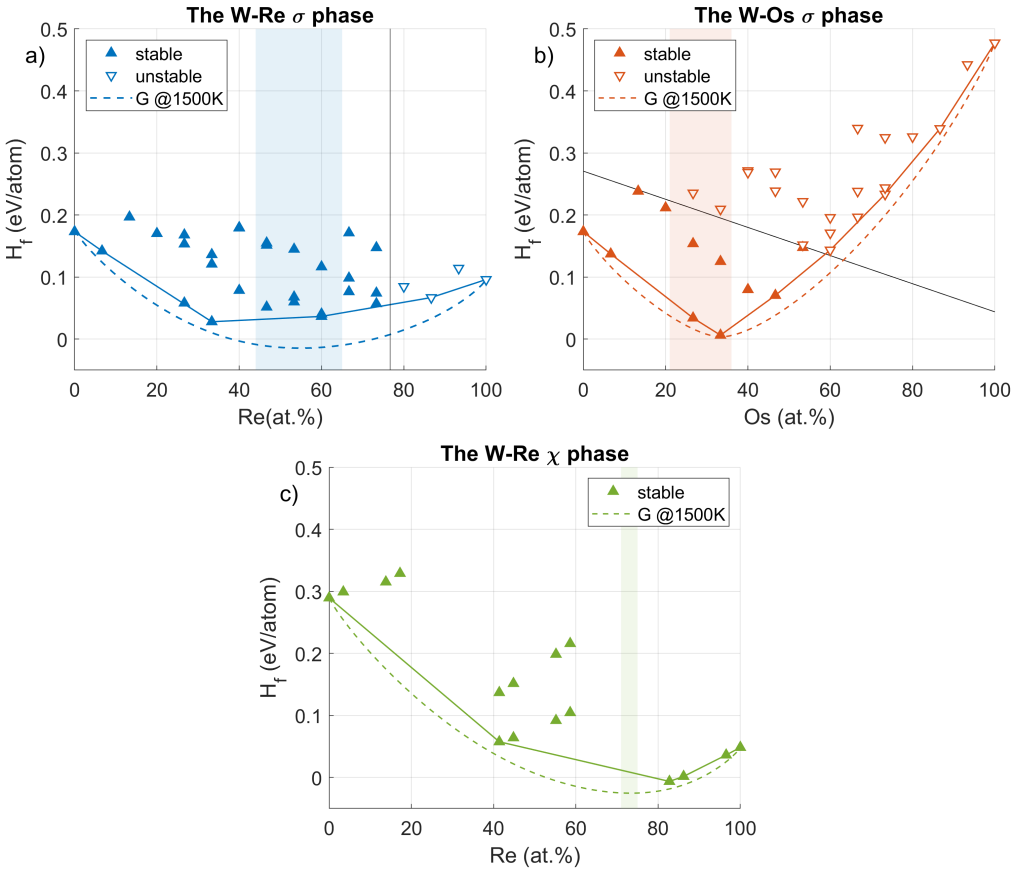

Figure 7: Formation enthalpy at 0 K for the 32 sublattice configurations of (a) W–Re and (b) W–Os σ phase and for the 16 configurations of (c) the W–Re χ phase. Filled symbols indicate dynamically stable configurations, whereas hollow markers indicate dynamically unstable ones. The black line is the optimal boundary separating stable from unstable configurations. The convex hulls are drawn with solid lines, and the dashed lines indicate the free energy at 1500 K. The colored backgrounds indicate the thermodynamically stable concentrations at 1500 K according to [28].

demonstrate that the method can accurately predict Wyckoff site occupations. It is further shown how chemical composition and configurational entropy affect the stability of the phases. In particular, the dynamic stability of the σ phase is shown to depend on Re/Os concentration and lattice site occupation.

The H_f at 0 K of the sublattice configurations is plotted against the transmutation product content in Figure 7. The convex hulls of the phases are computed using the common tangent method. The concentrations at which the phases are thermodynamically stable at 1500 K, according to their phase diagrams,

are marked with colored backgrounds [28]. The configurations of lowest H_f are when Re/Os occupies the low coordination sites, i.e. the $2a$ and $8i_2$ sites in the σ phase and the $24g_1$ and $24g_2$ sites in the χ phase, see the unit cells in Figure 2. The composition of these configurations is referred to as the ideal composition [59] and correspond to 33.3 at.% Re/Os for σ and 82.9 at.% Re for the χ phase. For concentrations above and below the ideal ratio, the H_f values on the convex hull increase, indicating a gradual reduction in bonding strength. None of the σ configurations exhibit negative H_f values at 0 K, indicating that they are not thermodynamically stable at absolute zero temperature. However, in Paper IV, the vibrational contribution to the free energy was computed for the σ configurations, which indicated that the configurations at the ideal composition become thermodynamically stable for temperatures above 1050 K for W–Re and 130 K for W–Os. Furthermore, it was shown that the scatter in energy of configurations with the same stoichiometry reduces with temperature, indicating increased disorder at high temperatures as the cost of substituting atoms between sublattices reduces. Configurational entropy in the form of ideal mixing on the sublattices also plays a significant role in stabilizing phases at elevated temperatures. To illustrate its influence, the free energy according to Eq. (30) at 1500 K has been drawn with dashed lines in Figure 7. In addition to lowering the free energy, the minimum of the free energy shifts from the ideal composition and aligns more closely with the stable concentrations of the phases [28].

The scatter of H_f among configurations with the same stoichiometry is larger for W–Os than for W–Re, indicating that substituting atoms between the sublattice sites requires a higher energy cost for W–Os. The effect of this is seen in Figure 8, where the preferred atomic fractions of Re and Os on the Wyckoff sites are plotted as functions of the overall Re/Os concentrations. Experimental data obtained from W–Re σ precipitates in neutron-irradiated W samples are included in Figure 8(a) [26]. It can be seen that the sublattice model is in good agreement with the experimental data. In the σ phase, Os exhibit a more distinct preference for the low coordination sites than Re. For instance, at the ideal concentration, the W–Os σ phase is nearly fully ordered, with Os occupying the $2a$ and $8i_2$ sites. Only when the Os concentration exceeds 33 at.% does the excess of atoms compel Os to occupy the other sites.

To illuminate the underlying reasons behind the preferred Wyckoff site occupations, an analysis of the electron density of states (EDOS) of W–Os and W–Re σ configurations with identical stoichiometry but different site occupations was conducted in Paper III. It was discovered at configurations where Re/Os occupies $2a$ and $8i_2$ sites, that the EDOS near the Fermi level is lower,

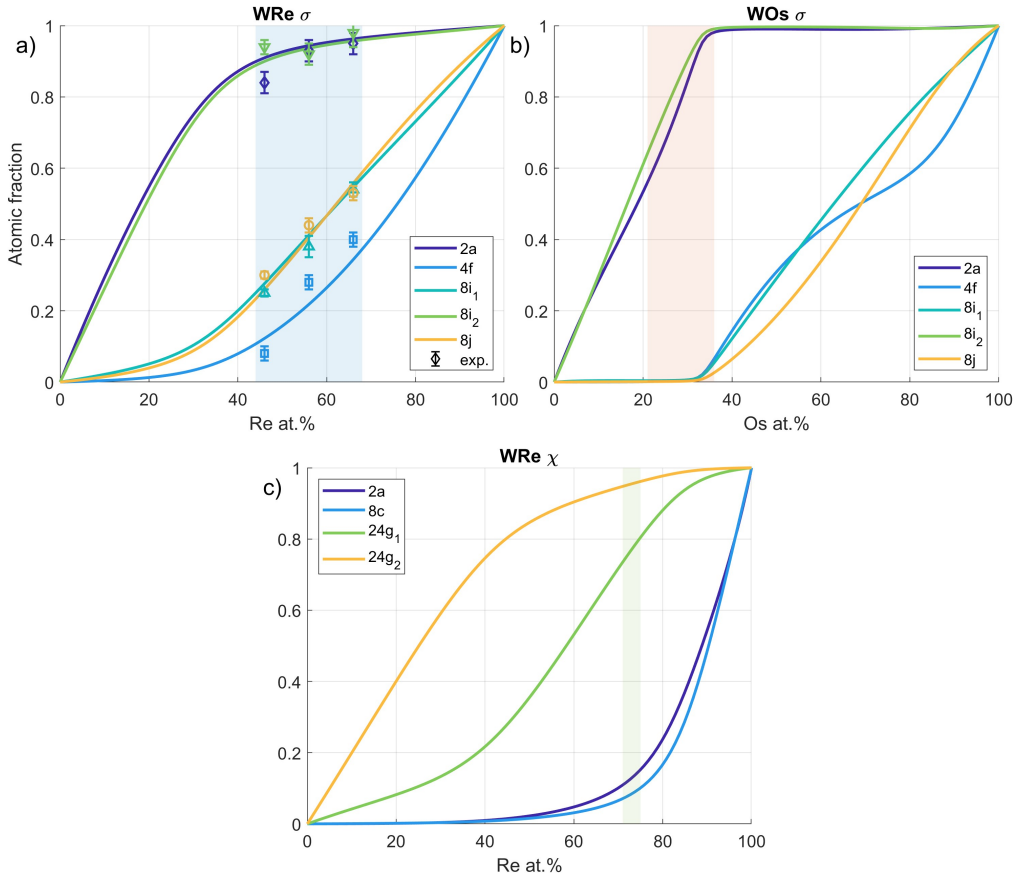

Figure 8: The atomic fraction of Re (or Os for the W–Os phase) on the Wyckoff sites of (a) the W–Re, (b) W–Os σ phase, and (c) the W–Re χ phases according to the sublattice model at T =1500 K. The concentrations at which the phases are thermodynamically stable according to the phase diagram are indicated with colored backgrounds [28]. The Wyckoff sites are color-coded with the same colors shown in the unit cells (see Figure 2). Experimental results for the W–Re σ phase are adopted from [26].

and the bonding peaks shift to lower energies, indicating stronger bonds and higher phase stability. The effects were more pronounced for the W–Os phase than for W–Re, indicating a stronger preference of Os for the low coordination site, as also can be seen in Figure 8. These results align well with the theories of the ordering of the σ and χ phases found in the literature [27, 59, 63, 64]. For example, in the σ phase, the near-icosahedral symmetry of the $2a$ and $8i_2$ sites are expected to cause d-orbital degeneracy [27]. This means that elements with half-filled d-orbitals (i.e. W) would have a high EDOS when occupying the sites [27]. Elements with filled or nearly filled d-orbitals (i.e., Os and Re)

generally have fewer electron states near the Fermi level [26, 63]. Therefore, the occupation of the $2a$ and $8i_2$ sites by Os or Re is preferred as it reduces the EDOS degeneracy near the Fermi level. The d-orbitals of Os are closer to being full than Re, which may explain why Os exhibits a stronger preference for the $2a$ and $8i_2$ sites. Geometric factors have also been suggested to influence Wyckoff site preference [65]. According to Frank's theory of metallic topological close-packed phases [59], the larger element prefers to occupy the more spacious lattice sites to reduce atomic size mismatch. In terms of the σ phase, smaller atoms would prefer the compact $2a$ and $8i_2$ sites, while larger atoms occupy the more spacious $4f$, $8i_1$, and $8j$ sites [66]. While the results are in line with the theory, given the minor differences in atomic radius (W: 1.93 Å, Re: 1.88 Å, Os: 1.85 Å [67]) and minimal changes in internal coordinates observed during relaxation, electronic factors likely dominate over size effects in regards to the ordering of the W–Re and W–Os σ phases.

The dynamic stability of the configurations is indicated in Figure 7. While all χ configurations are dynamically stable, several σ configurations are dynamically unstable. The dynamically stable and unstable configurations are linearly separable, with the optimal boundaries shown in Figure 7 determined using a Support Vector Machine algorithm [68]. The dynamic stability depends in part on the H_f and Re and Os concentration as there are no stable configurations above 73 at.% Re and 53 at.% Os and the unstable configurations lie in the regions of high H_f and/or high Re/Os content. The EDOS spectrum of the unstable configurations exhibited peaks at the Fermi level, which can be indicative of dynamic instability, as discussed in Paper IV. The connection between transmutation product concentration and the dynamic stability is suggested to be caused by the additional d-electrons of Re and Os, which increase the electron density at the Fermi level. If so, the extra d-electron of Os may explain why the instability occurs at lower Os concentrations than at Re concentrations, and shows how subtle differences in d-orbital filling can drastically change the dynamic stability of the σ phase. It was also discovered that dynamic stability depends on Wyckoff site occupations. Configurations where Re occupies all of the $8i_1$, $8i_2$, and $8j$ sites, or when Os occupies the $8j$ sites, were all dynamically unstable. The effects and consequences of this are discussed further in section 3.3.

The discussion above indicates that the difference in d-orbital filling has a significant influence on the stability and Wyckoff site occupation of the W–Re and W–Os σ phase. The result of this is a W–Os σ phase that becomes dynamically unstable at lower concentrations of transmutation products and is highly ordered regarding Wyckoff site occupation at the ideal concentration compared

to the W–Re σ phase. Previous studies have shown that disorder in the σ phase weakens the bond strength [66, 69]. The bond strength of a material affects its mechanical and fracture properties, as will be discussed in the next section.

3.2 Mechanical and fracture-related properties

To study the mechanical properties, the elastic constants of the phases are computed using DFT, which are then used to calculate the Voigt averages of the bulk (K_V), shear (G_V), and Young's modulus (E_V) of the phases, and to estimate the Vickers hardness (H_V) using an empirical relation [70]. As in the previous section, the dependency of the transmutation product concentration is estimated using the sublattice model as described in section 2.5. Knowing the concentration dependency is beneficial as the σ and χ phases are known to crystallize in a wide range of compositions.

In Figure 9, the elastic properties at 0 K of the phases are plotted as a function of the transmutation product concentration. The phases exhibit similar values and behavior of K_V, which monotonically increases with increasing Re/Os content. For the behavior of C_{44} and the parameters depending on it, that is G_V, H_V and E_V, the W–Os σ phase exhibit distinct peaks at the ideal composition followed by a significant softening of the parameters at high Os contents, which was not observed for the W–Re phases. The W–Os σ phase is significantly harder than the W–Re phases; The average values of H_V and E_V of the σ and χ phases in the thermodynamically stable concentration ranges are high, that is 11.7 GPa and 384 GPa for W–Os σ phase, 7.9 GPa and 336 GPa for the W–Re σ phase, and 3.7 GPa and 270 GPa of the W–Re χ phase. The difference in mechanical behavior between the W–Os and W–Re phases is linked to differences in the Wyckoff site occupation and formation enthalpy, which have a direct influence on the mechanical and fracture-related properties. At the ideal composition where the W–Os σ phase is highly ordered and most stable, the phase exhibits peak values of G_V, which is a better indicator of bonding strength than K_V due to the conserved volume under shear deformation [62]. Previous studies on the σ phase have also found a positive correlation between the order of the σ phase and the bond strength [66, 69]. On the contrary, the W–Re phases exhibit a higher amount of disorder at their ideal compositions and, therefore, do not exhibit clear peaks at the ideal composition. Furthermore, the dependency of the mechanical properties on the Re content is, in general, weaker than for the W–Os phase.

In addition to affecting the resistance to shearing, the value of C_{44} influences mechanical stability. Above Os concentrations 78 at.%, the σ phase becomes

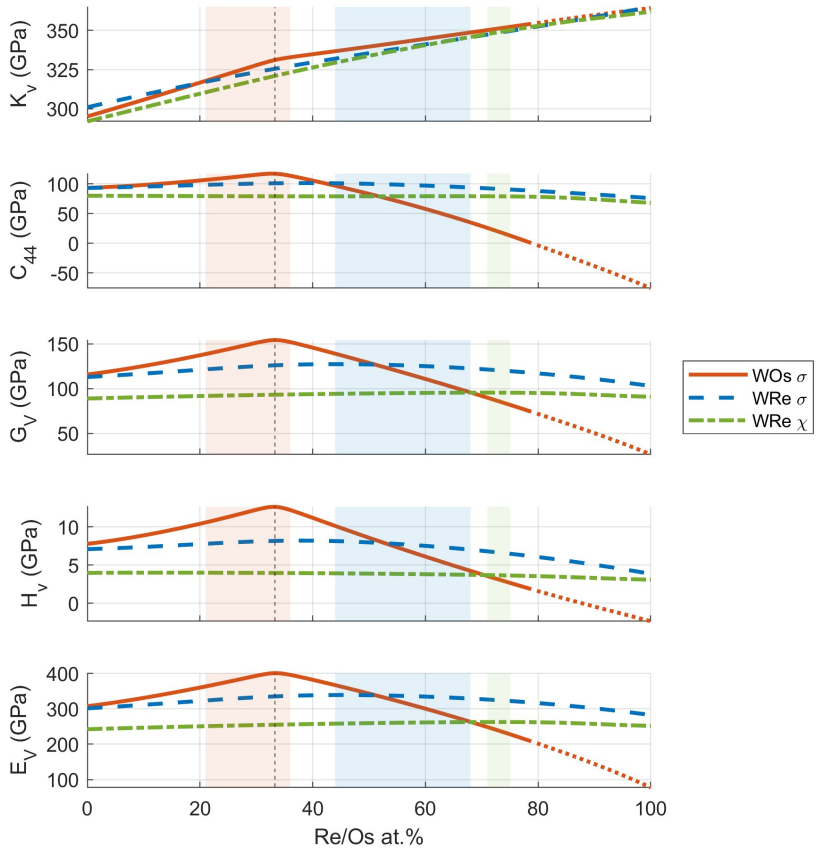

Figure 9: Hardness and elastic moduli at 0 K of the σ and χ phases as a function of the transmutation product content. The gray dashed line indicates the ideal composition of the σ phase. The colored backgrounds indicates where the phases are thermodynamically stable at 1500 K according to [28]. The W–Os σ phase becomes mechanically unstable at high Os concentrations, indicated by the transition to dotted lines.

mechanically unstable according to the Born stability criteria, indicated by negative values of C_{44}, shown by dotted lines in Figure 9. The mean value of G_V in the stable concentration ranges is for the W–Os σ phase 148 GPa, for the W–Re σ phase 125 GPa, and for the W–Re χ phase 95 GPa. By comparison, the DFT value of G_V for BCC W at 0 K is 148 GPa. A shear modulus mismatch between the precipitate and a surrounding matrix can cause modulus hardening due to the strain field generated by the mismatch interacting with dislocation motion [71]. However, it should be noted that modulus hardening is a relatively weak effect compared with other mechanisms of precipitation hardening [72] and, except for the χ phase, the mismatch is small. Modulus hardening may, therefore, not be the primary cause behind the precipitation hardening

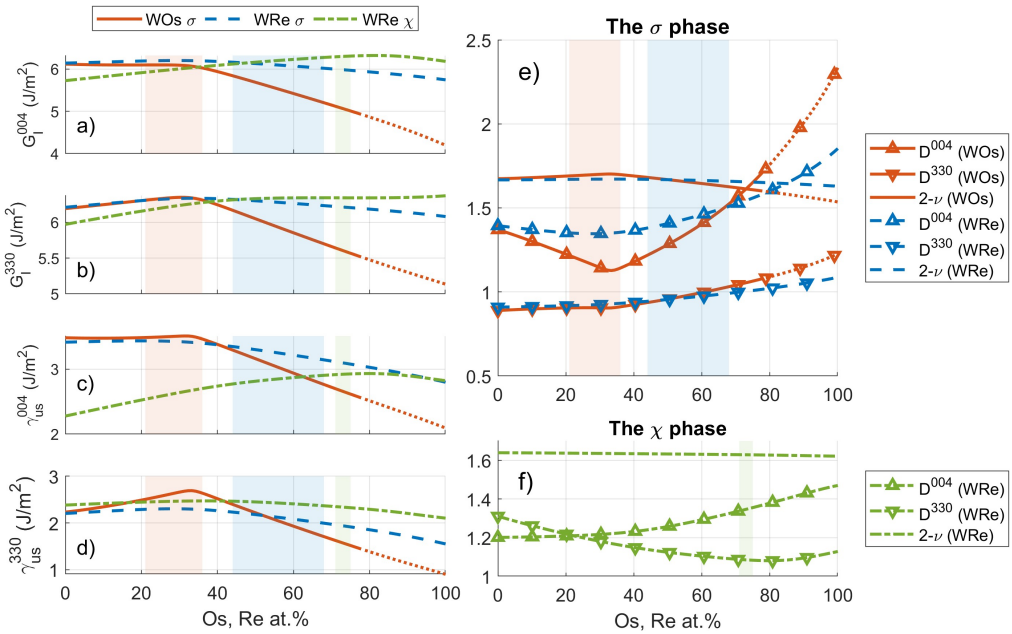

Figure 10: The fracture-related properties at 0 K of the W–Os σ phase (solid lines), the W–Re σ phase (dashed lines), and the W–Re χ phase (dash-dotted lines). The colored background indicate where the phases are thermodynamically stable [28]. In (a)-(b) the brittle energy release rate, G_I, and (c)-(d) the unstable stacking fault energy, γ_{us}, are shown, while in (e) the Rice ductility parameters D^{004} and D^{330} of the {004} and {330} crack planes are plotted. It can be seen that the two ductile fracture criteria of 4 and $4 \times (2 - \nu)$ are not met.

of the W-based components. A stronger mechanism of precipitation hardening occurs when non-deformable precipitates act as impenetrable obstacles, providing strong pinning of dislocation motion [73, Chapter 13], thereby reducing the ductility of the host material. This mechanism of precipitation hardening has been documented for the W–Re σ and χ precipitates through molecular dynamics (MD) simulations [74, 75]. Conducting similar studies on the W–Os phase would provide valuable insights into the precipitation hardening observed experimentally. However, a computationally efficient MD potential for W–Os is necessary for such research, which will be discussed further in section 4.2.

In Figure 10(a)-(d) the concentration-dependent G_I and γ_{us} of the {004} and {330} close-packed planes are shown for the σ and χ phases. Like the elastic properties, the fracture-related properties of the W–Os σ phase deviate from the W–Re phases as they exhibit significant softening for Os concentrations beyond 33 at.%. For high Os contents where the bond strength is weak, the separation

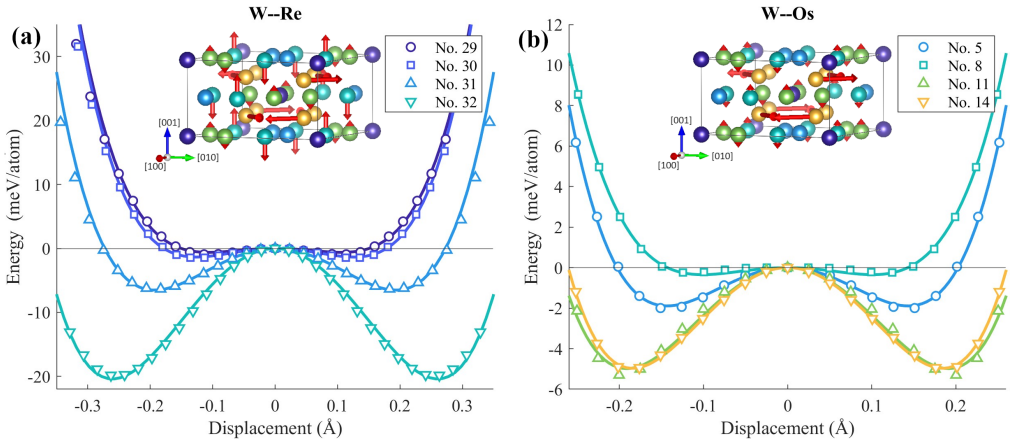

Figure 11: Potential energy surfaces versus displacement along the imaginary modes shown in the insets (amplitudes are enhanced for clarity) for the (a) W–Re and (b) W–Os σ phase. The numbers in the legend refer to different σ configurations; see Paper IV. The x-axis indicates the displacement of the $8j$ atoms. The data points, indicated with symbols, provide a good fit for the Landau double-well potential drawn with solid lines.

resistance of close-packed planes, indicated by G_I^{004} and G_I^{330}, reduces and the values of γ_{us}^{004} and γ_{us}^{330} decreases indicating that the energy required for bond breaking goes down. For both the σ and χ phases, the $\{330\}$ planes have lower values of γ_{us}, indicating that they are preferred over the $\{004\}$ planes for ductile mechanisms such as slip and twinning. The ductility parameters for different combinations of slip systems and crack planes are plotted as a function of transmutation product content in Figure 10(e) for σ and (f) for χ. Brittle fracture behavior is predicted for the σ and χ phases, as the criteria in Eqs. (27) and (28) are not fulfilled. That is, the value of D^{004} remains below 4.0 for all concentrations, and the value of D^{330} stays below the $4 \times (2 - \nu)$ limit. However, high transmutation product contents improve the ductility somewhat, especially for the W–Os σ phase, as seen by the increase of the D^{004} and D^{330} parameters. The intrinsic brittleness of the phases is a crucial piece of knowledge, as brittle precipitates can initiate points of cracking [17].

3.3 Phase transformation in the σ phase

In Paper IV it was discovered that the dynamic stability of the σ phase depends both on the Re/Os concentrations and on the Wyckoff site occupation. As dynamically unstable crystals tend to spontaneously transform into stable or

metastable crystals, it is compelling to search for what new stable structure the σ phase might transform into. For this investigation, the imaginary modes of the phase were used as a starting point.

The four unstable W–Re σ configurations all have Re occupying the $8i_1$, $8i_2$, and $8j$ Wyckoff sites (see, Figure 2) and share a common imaginary mode that features vibrations of the sites $8i_1$ and $8i_2$ in direction [001] and $8j$ in directions [110] and [1$\bar{1}$0]. The mode is illustrated in Figure 11(a), and the potential energy surface of the mode is plotted for the four configurations. The DFT data provide a good fit to the Landau double-well potential, indicating dynamic instability. Several of the W–Os σ configurations were unstable. In this section, the focus will be on configurations with Os occupying only the $8j$ site, as all of these are dynamically unstable, even at low Os concentrations. These configurations also share an imaginary mode that is very similar to the one observed for the W–Re configurations, although with a significantly larger amplitude of the $8j$ sites relative to the $8i_1$ and $8i_2$ sites, as illustrated in Figure 11(b). The potential energy surfaces resulting from the mode are plotted for selected W–Os configurations.

The unstable W–Os configuration, with Os occupying only the $8j$ site, was selected for further investigation because it lies within the concentration range where the σ phase is predicted to be thermodynamically stable. A new, dynamically stable crystal structure with a slightly lower formation enthalpy was discovered following a series of full relaxations initiated from the bottom of the left well in Figure 11. The new orthorhombic crystal structure, belonging to the $Pnn2$ space group, has lower symmetry than the tetragonal σ phase. Such symmetry-lowering transitions to lower energy states are not uncommon and are found in iron-based superconductors [76, 77], rare earth manganites [78, 79], and via the Jahn-Teller effect in ZrH_x and TiH_x [80–82]. The computed diffraction patterns and unit cells are visualized in Figure 12 for (a) the tetragonal σ lattice and (b) the new orthorhombic crystal lattice. While the diffraction patterns of the structures are similar, the orthorhombic structure exhibits several cases of peak splitting as a consequence of the lower symmetry.

In Figure 13, the phonon band structure of the tetragonal σ configuration and orthorhombic phase is shown. The imaginary modes of the σ phase are structurally associated with the $8j$ sites occupied by Os, as seen from the projected PDOS in Figure 13(a). The phonon band structure of the dynamically stable orthorhombic structure is shown in Figure 13(b). Comparing EDOS of the tetragonal and orthorhombic W–Os phases in Figure 13(c) and (d), the orthorhombic deformation splits the peak at the Fermi level from the $8j$ Os atoms in the σ phase into two, thereby forming a local minimum and reducing the Os d-electron

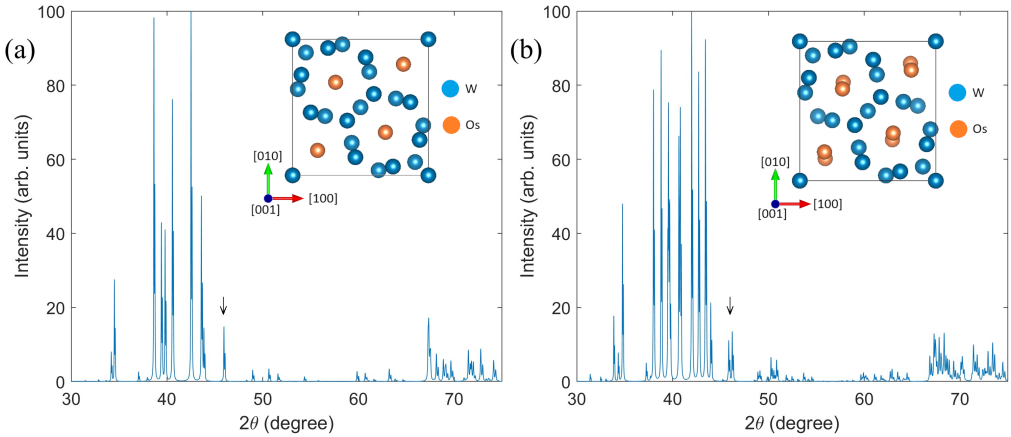

Figure 12: Diffraction pattern of (a) the tetragonal σ phase with Os on the $8j$ sites and (b) the orthorhombic phase. The unit cells are inserted with color-coded W and Os atoms. An example of peak splitting is indicated by an arrow.

degeneracy at the Fermi level. This suggests an electronic stabilization mechanism reminiscent of the Jahn-Teller effect seen in TiH_x and ZrH_x, in which tetragonal deformations reduce the electron degeneracy at the Fermi level [80–82, 82–84]. Although the orthorhombic phase is mechanically and dynamically stable, its positive formation enthalpy makes it likely metastable. Nonetheless, such phases could form under the extreme, non-equilibrium conditions experienced by neutron-irradiated plasma-facing components. Further research is needed to understand how the new orthorhombic precipitates affect mechanical properties, particularly ductility, in W-based PFCs, for example, by using MD simulations to estimate the impediment of dislocations by the precipitate.

3.4 Thermal expansion of the W–Re σ and χ phases

Tungsten-based PFCs are required to operate over large temperature ranges and cyclic thermal loading [3]. A significant mismatch in thermal expansion between the W matrix and σ and χ precipitates may induce thermal stresses and promote fatigue failure, posing a challenge to the longevity of the PFC. As there are no experimental data on the CTE of the W–Re σ and χ, estimates based on computational methods are employed. In this section, the CTE of the W–Re σ and χ phases is estimated using the QHA and the acoustic-based DG model.

To benchmark the accuracy of the calculations, the volumetric CTEs of BCC W and HCP Re are compared with experimental data in Figure 14. The QHA

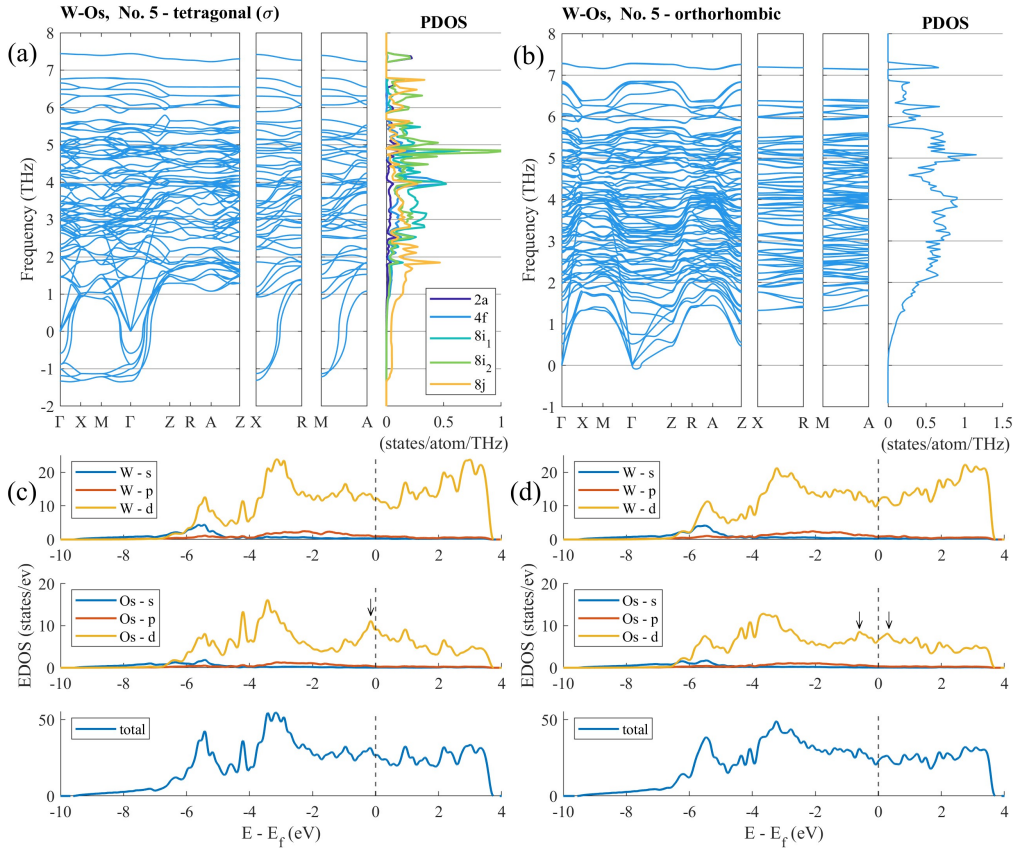

Figure 13: Comparison of the phonon dispersion structure and PDOS of W–Os in (a) the tetragonal σ phase and (b) the orthorhombic phase. The PDOS are projected onto the Wyckoff sites of σ phase. The EDOS of the W and Os atoms projected onto the *s*-, *p*-, and *d*-orbitals as well as the total EDOS for (c) the σ phase and (d) the orthorhombic phase. The arrows indicate peaks near the Fermi level.

results are in good agreement with experiments: the predicted values of BCC W and HCP Re are 13% and 5% larger, respectively, than the experimental values at 1000 K, where the deviation is largest. The deviation at high temperatures may be due to anharmonic effects excluded in the QHA, such as phonon-phonon interaction, which may become significant at high temperatures. The DG model, in contrast, captures the CTE of Re poorly, which has also been found in other studies [87, 88]. It has been suggested that this is due to the acoustic approximation that the DG model is based on[88], as optical modes contribute differently to the thermal expansion than acoustic [89]. The phonon band structure of BCC W does not contain any optical phonon modes, and here, the DG method produces results in reasonable agreement with experiments. Since the σ and

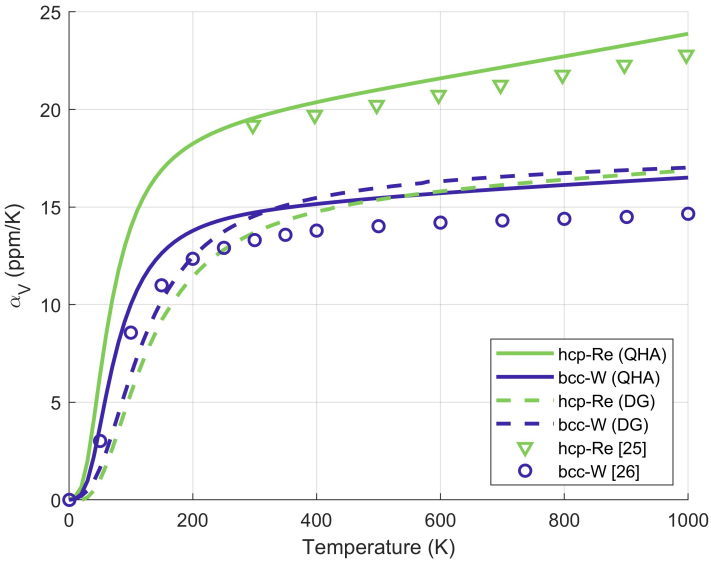

Figure 14: Coefficient of thermal expansion as a function of temperature for BCC W, HCP Re, and the most stable σ and χ sublattice configurations estimated using QHA (solid lines) and DG (dashed lines). Experimental data adopted from [85, 86] are shown as symbols.

χ phases contain multiple optical phonon modes, the applicability of the DG model to these phases comes into question.

In Figure 15, the CTE of selected σ and χ sublattice configurations on the convex hull with varying Re content are plotted. These configurations are chosen for their low formation enthalpy. In the σ phase, the CTE is determined only for structures with up to 60 at.% Re, as no dynamically stable configurations exist on the convex hull at higher concentrations. The QHA predicts a nonlinear trend of increasing CTE with increasing Re content. These results align with experimental data and DFT calculations on BCC W with high concentrations of solute Re, where the CTE also increases with increasing Re content [46, 90]. At high temperatures and Re concentrations, the value of CTE becomes more sensitive to temperature fluctuations, as indicated by the more pronounced slope of the CTE curves.

An analytical expression of the CTE as a function of T and Re concentration was constructed in Paper II and fitted to the QHA data on the σ and χ configurations. The function is shown in Figure 16. To gauge the size of the CTE mismatch between precipitates and the surrounding BCC W material, the function is utilized to compute the average CTE of the phases in their stable

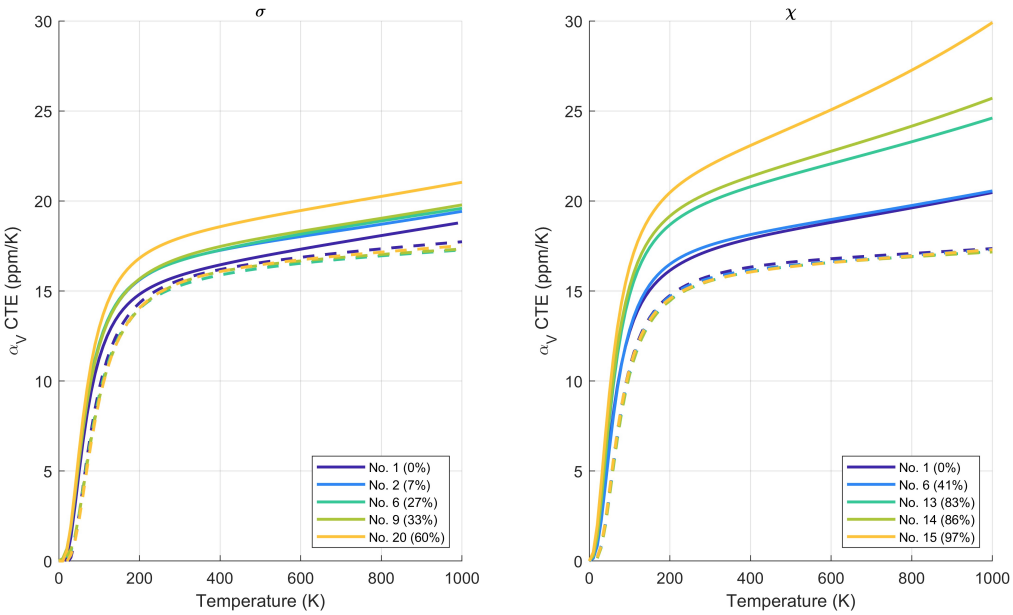

Figure 15: The CTE for (a) σ and (b) χ sublattice configurations as predicted by QHA (solid line) and DG (dashed line). The legend indicates the configuration number and the atomic percentage of Re in the configuration.

concentration ranges. By comparing with experimental data for BCC W, the mismatch in volumetric CTE is estimated to be ∼32% for σ type precipitates and ∼42% for the χ phase at 300 K. At 1000 K, the mismatch increases to ∼42% and ∼62% for σ and χ phase, respectively [91]. This suggests that χ precipitates, due to their higher Re content, contribute more significantly to thermal stress buildup than the σ phase. It should be noted that the thermally induced stress field depends on the morphology and size of the precipitates in addition to the CTE mismatch. The surroundings of the precipitates also affect the thermal stresses. For example, one study found that χ phase precipitates are often located in connection with irradiation-induced voids [20], which may alleviate some of the thermal stress buildup. The study also found that the precipitates are surrounded by "clouds" of high concentrations of transmutation products [20]. While this may reduce the CTE mismatch to some degree, the mismatch is still considerable. For example, if the surrounding BCC W matrix contains 25 at.% Re, which is close to the solubility limit, its experimental CTE value is 16.1 ppm/K at 1000 K [90], resulting in a reduction of the mismatch with the χ from ∼62% to ∼48%. To gain deeper insight into the thermo-mechanical consequences of the mismatch, the CTE data provided in this thesis work can be used as input for large-scale modeling, such as phase-field [92] or finite element

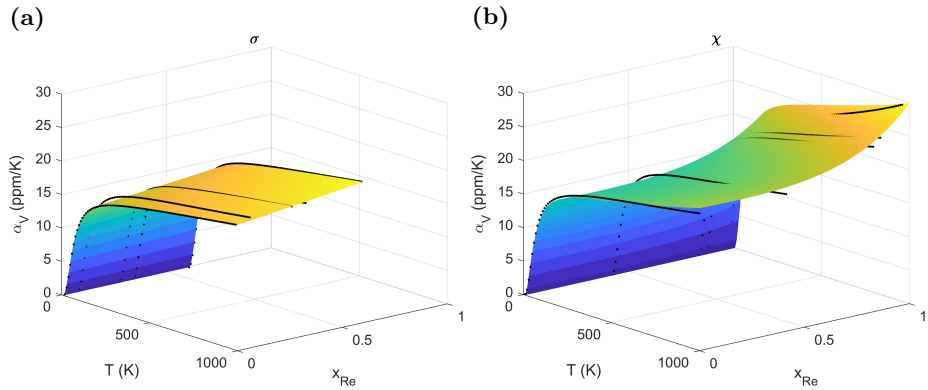

Figure 16: The CTE of the σ and χ phase. The black dots show the CTE of the configurations in Figure 15 while the surfaces show the fitted functions with parameters given in Paper II.

simulations [93].

4 Conclusions and outlook

4.1 Main conclusions

In this thesis work, several intrinsic properties, including stability, elastic and fracture properties, and thermal expansion, of the W–Re and W–Os σ and χ phases have been investigated using first-principles calculations.

Using the sublattice model, the structure, lattice site occupation, and formation enthalpy were obtained. At zero absolute temperature, the lowest formation enthalpy is observed for configurations where Re and Os occupy the low coordination number sites of the structures. Only for the W–Re χ phase, is this configuration thermodynamically stable at 0 K. However, when the vibrational free energy is accounted for, the σ phase configurations at the ideal composition become thermodynamically stable at 1050 K for W–Re and 130 K for W–Os, indicating thermally induced stability. Additionally, including the configurational entropy contribution to the free energy changes the stable Re and Os concentrations to values more closely aligned with the stable concentration ranges in their phase diagrams.

Analysis of the EDOS indicated that due to differences in the *d*-orbital filling, Os exhibits a stronger preference for the low coordination number sites of the

σ phase than Re, resulting in the phase being almost completely ordered at the ideal composition. It was revealed that this caused the mechanical and fracture-related properties of the W–Os σ phase to exhibit a higher dependency on the chemical composition than for the W–Re phases. At the ideal composition, where the phase is highly ordered in terms of Wyckoff site occupation, the W–Os σ has peak values of Vickers hardness, Young's modulus, and shear modulus, well above the W–Re σ and χ phase, indicating stronger atomic bonds. As hard, non-deformable precipitates impede dislocation motion [73, Chapter 13], the W–Os phase may therefore act as a stronger obstacle to dislocation movement than what has been estimated for the W–Re phases [74]. For high Os content where the disorder in the phase increases as Os starts to occupy unfavorable Wyckoff sites, the parameters of the W–Os σ phase exhibit strong softening, resulting in the phase becoming mechanically unstable for Os concentrations exceeding 78 at.% according to Born's stability criteria. To the best of the author's knowledge, the strong impact of the *d*-orbital filling on the mechanical properties and stability of the σ phase has not previously been documented in the literature. This finding may be relevant for other topologically close-packed phases. From Rice's theory of ductile fracture, the σ and χ phases are expected to exhibit brittle fracture behavior for all Re and Os concentrations. This is a concern for the durability of W-based PFCs, as brittle precipitates can initiate points of cracking [17].

It was further discovered that the chemical composition and Wyckoff site occupation also affect the dynamic stability of the σ phase. The W–Re σ phases become dynamically unstable for concentrations above 73 at.% Re and W–Os phase becomes unstable for concentrations above 53 at.% Os. In terms of Wyckoff site occupation, the W–Re phase is dynamically unstable when Re occupies the $8i_1$, $8i_2$, and $8j$ sites, while instability of the W–Os phase occurs when Os occupies the $8j$ Wyckoff sites. These unstable configurations share an imaginary mode that exhibits large vibrations of the $8j$ sites in the [110] and [1$\bar{1}$0] crystallographic directions. Using a W–Os configuration as a representative model, it was found that this mode led to transformation to a new orthorhombic phase of lower symmetry, belonging to the $Pnn2$ space group. To the best of the author's knowledge, this phase has not been previously described for the W–Os system. These results provide further knowledge of the formation of W–Re and W–Os σ precipitates and can, e.g., be incorporated into phase diagram studies of the W, Re, and Os system.

The CTE of the W–Re σ and χ phases was estimated for the first time in this thesis. An analytical function of the CTE and its dependence on the Re content and temperature was obtained using dynamically stable configurations

on the convex hull. It was discovered that within their stable concentration regions, the σ and especially the χ precipitates may have a significant mismatch in CTE compared to the surrounding W matrix. This may lead to thermally induced stresses and subsequent crack formation, which could compromise the longevity of W-based components. However, as the stress field of a precipitate also depends on the morphology and surroundings, further studies, on a larger length scale than DFT, are needed to assess the full effects of the CTE mismatch.

4.2 Suggested future work

While first-principles methods provide accurate results for the properties of the σ and χ phases, the high computational cost of DFT calculations limits the study to only several dozen or hundreds of atoms. However, most precipitation hardening effects stem from the interaction between the precipitates and other crystal defects, such as dislocations and grain boundaries. To capture these hardening effects, simulations involving the interaction of tens to hundreds of thousands of atoms are required. While this is well beyond the capabilities of DFT, the results in this thesis provide a useful basis for larger-scale simulations.

Large-scale studies on the impediment of dislocation movement by W–Re precipitates in W have been carried out using MD simulations [74, 75]. As the W–Os σ phase exhibits significantly different mechanical properties, such as increased hardness and shear modulus, equivalent studies on the W–Os phase would provide valuable insights into the mechanisms of the experimentally observed precipitation hardening. The orthorhombic W–Os phase observed in this thesis work should also be included to gain a complete picture. An accurate and computationally efficient interatomic potential for the W–Os system is essential for reliable MD simulations. Machine-learned interatomic potentials offer a promising solution, as they have demonstrated the ability to reproduce DFT data with high accuracy at a significantly reduced computational cost [94–96]. The DFT data generated in this thesis can serve as a foundation for both fitting and evaluating such machine-learned potentials.

The thermal stresses induced by the mismatch in CTE between precipitates and the W matrix also require large-scale simulations to evaluate their effects and consequences. For this purpose, finite element simulations can be employed. The DFT data on the Re-dependent CTE of the W–Re phases can be utilized as input for such modelling. Combined with experimental data on the size and morphology of the precipitates, the thermal strain fields can be evaluated under various thermal conditions.

References

[1] R. G. Abernethy. Predicting the performance of tungsten in a fusion environment: a literature review. *Mater. Sci. Technol.*, 33:388–399, 2017. ISSN 0267-0836.

[2] G. McCracken and P. Scott. *Fusion: The energy of the universe*. Elsevier, 2005.

[3] J. Linke, J. Du, T. Loewenhoff, G. Pintsuk, B. Spilker, I. Steudel, and M. Wirtz. Challenges for plasma-facing components in nuclear fusion. *Matter Radiat. Extremes*, 4:056201, 2019.

[4] ITER Organization. Technical gallery. URL `https://www.iter.org/iter-image-galleries/technical`.

[5] H. Bolt, V. Barabash, W. Krauss, J. Linke, R. Neu, S. Suzuki, N. Yoshida, and ASDEX Upgrade Team. Materials for the plasma-facing components of fusion reactors. *J. Nucl. Mater.*, 329:66–73, 2004.

[6] V. Philipps. Tungsten as material for plasma-facing components in fusion devices. *J. Nucl. Mater.*, 415(1):S2–S9, 2011.

[7] N. Noda, V. Philipps, and R. Neu. A review of recent experiments on W and high Z materials as plasma-facing components in magnetic fusion devices. *J. Nucl. Mater.*, 241:227–243, 1997.

[8] G. F. Matthews, JET EFDA Contributors, ASDEX-Upgrade Team, et al. Plasma operation with an all metal first-wall: comparison of an ITER-like wall with a carbon wall in JET. *J. Nucl. Mater.*, 438:S2–S10, 2013.

[9] S. Krat, Y. Gasparyan, A. Pisarev, I. Bykov, M. Mayer, G. de Saint Aubin, M. Balden, C. P. Lungu, and A. Widdowson. Erosion at the inner wall of JET during the discharge campaign 2011-2012 in comparison with previous campaigns. *J. Nucl. Mater.*, 456:106–110, 2015.

[10] J. Fellinger, M. Richou, G. Ehrke, M. Endler, F. Kunkel, D. Naujoks, Th. Kremeyer, A. Menzel-Barbara, Th. Sieber, J. F. Lobsien, et al. Tungsten based divertor development for Wendelstein 7-X. *Nucl. Mat. Energy*, 37: 101506, 2023.

[11] N. Holtkamp, ITER Project Team, et al. An overview of the iter project. *Fusion Eng. Des.*, 82(5-14):427–434, 2007.

[12] P.-H. Rebut et al. ITER: the first experimental fusion reactor. *Fusion Eng. Des.*, 27:3–16, 1995.

[13] R. G. Abernethy, J. S. K. L. Gibson, A. Giannattasio, J. D. Murphy, O. Wouters, S Bradnam, Packer L. W., M. R. Gilbert, M. Klimenkov, M. Rieth, H. C. Schneider, C. D. Hardie, S. G. Roberts, and D. E. J. Armstrong. Effects of neutron irradiation on the brittle to ductile transition in single crystal tungsten. *J. Nucl. Mater.*, 527:151799, 2019.

[14] T. Tanno, M. Fukuda, S. Nogami, and A. Hasegawa. Microstructure development in neutron irradiated tungsten alloys. *Mater. Trans.*, 52:1447–1451, 2011.

[15] G. A. Cottrell, R. Pampin, and N. P. Taylor. Transmutation and phase stability of tungsten armor in fusion power plants. *Fusion Sci. Technol.*, 50:89–98, 2006.

[16] P. L. Raffo. Yielding and fracture in tungsten and tungsten-rhenium alloys. *J. Less Common Met.*, 17(2):133–149, 1969.

[17] Y. Nemoto, A. Hasegawa, M. Satou, and K. Abe. Microstructural development of neutron irradiated W-Re alloys. *J. Nucl. Mater.*, 283-287: 1144–1147, 2000.

[18] R. K. Williams, F. W. Wiffen, J. Bentley, and J. O. Stiegler. Irradiation induced precipitation in tungsten based, W-Re alloys. *Metall. Trans. A*, 14:655–666, 1983.

[19] M. Fukuda, K. Yabuuchi, S. Nogami, A. Hasegawa, and T. Tanaka. Microstructural development of tungsten and tungsten–rhenium alloys due to neutron irradiation in hfir. *J. Nucl. Mater.*, 455(1-3):460–463, 2014.

[20] M. Dürrschnabel, M Klimenkov, U. Jäntsch, M. Rieth, H. C. Schneider, and D. Terentyev. New insights into microstructure of neutron-irradiated tungsten. *Sci. Rep.*, 11(7572), 2021.

[21] M. J. Lloyd, A. J. London, J. Haley, M. R. Gilbert, C. Becquart, C. Domain, E. Martinez, M. Moody, Paul Bagot, D. Nguyen-Manh, and D. Armstrong. Interaction of transmutation products with precipitates, dislocations and grain boundaries in neutron irradiated W. *Materialia*, page 101370, 2022.

[22] M. Klimenkov, M. Dürrschnabel, U. Jäntsch, P. Lied, M. Rieth, H. C. Schneider, D. Terentyev, and W. Van Renterghem. Microstructural analysis of w irradiated at different temperatures. *J. Nucl. Mater.*, 572:154018, 2022.

[23] M. R. Gilbert, S. L. Dudarev, S. Zheng, L. W. Packer, and J. Ch. Sublet. An integrated model for materials in a fusion power plant: transmutation, gas production, and helium embrittlement under neutron irradiation. *Nucl. Fusion*, 52:083019, 2012.

[24] E. O. Hall and S. H. Algie. The sigma phase. *Metall. Rev.*, 11(1):61–88, 1966.

[25] C.-C. Hsieh and W. Wu. Overview of intermetallic sigma (σ) phase precipitation in stainless steels. *Inter. Sch. Res. Not.*, 2012(1):732471, 2012.

[26] C. Berne, M. Sluiter, Y. Kawazoe, T. Hansen, and A. Pasturel. Site occupancy in the Re-W sigma phase. *Phys. Rev. B*, 64:144103, 2001.

[27] J.-C. Crivello, A. Breidi, and J.-M. Joubert. χ and σ phases in binary rhenium–transition metal systems: a systematic first-principles investigation. *Inorg. Chem.*, 52(7):3674–3686, 2013.

[28] T. B. Massalski, H. Okamoto, P. Subramanian, L. Kacprzak, and W. W. Scott. *Binary alloy phase diagrams*, volume 1. American society for metals Metals Park, OH, 1986.

[29] K. Momma and F. Izumi. VESTA 3 for three-dimensional visualization of crystal, volumetric and morphology data. *J. Appl. Crystallogr.*, 44(6): 1272–1276, 2011.

[30] E. B. Tadmor and R. E. Miller. *Modeling Materials*. Cambridge, 2011.

[31] F. Giustino. *Materials Modelling using Density Functional Theory*. Oxford University Press, 2014.

[32] W. Pauli. Über den zusammenhang des abschlusses der elektronengruppen im atom mit der komplexstruktur der spektren. *Z. Angew. Phys.*, 31(1): 765–783, 1925.

[33] P. Hohenberg and W. Kohn. Inhomogeneous electron gas. *Phys. Rev.*, 136 (3B):B864–B871, 1964.

[34] W. Kohn and L. J. Sham. Self-consistent equations including exchange and correlation effects. *Phys. Rev.*, 140(4A):A1133–A1138, 1965.

[35] W. Kohn. Nobel Lecture: Electronic structure of matter—wave functions and density functionals. *Rev. Mod. Phys.*, 71(5):1253, 1999.

[36] Z. Xing. *Investigation of oxidation machanisms in magnesium by density functional theory*. Doctoral thesis, Lund University, 2025.

[37] P. E. Blöchl. Projector augmented-wave method. *Phys. Rev. B*, 50:17953–17979, 1994.

[38] R. M. Martin. *Electronic Structure*. Cambridge University Press, 2004.

[39] N. A. W. Holzwarth, G. Matthews, R. B. Dunning, A. R. Tackett, and Y. Zeng. Comparison of the projector augmented-wave, pseudopotential, and linearized augmented-plane-wave formalisms for density-functional calculations of solids. *Phys. Rev.*, 55(4):2005, 1997.

[40] I. Pallikara, P. Kayastha, J. M. Skelton, and L. D. Whalley. The physical significance of imaginary phonon modes in crystals. *Electron. Struct.*, 4(3): 033002, 2022.

[41] M. Born and K. Huang. *Dynamical theory of crystal lattices*. Oxford university press, 1996.

[42] A. Togo. First-principles phonon calculations with phonopy and phono3py. *J. Phys. Soc. Jpn.*, 92(1):012001, 2023. doi: 10.7566/JPSJ.92.012001.

[43] A. Togo, L. Chaput, T. Tadano, and I. Tanaka. Implementation strategies in phonopy and phono3py. *J. Phys. Condens. Matter*, 35(35):353001, 2023. doi: 10.1088/1361-648X/acd831.

[44] F. Birch. Finite strain isotherm and velocities for single-crystal and polycrystalline NaCl at high pressures and 300 K. *J. Geophys. Res.: Solid Earth*, 83(B3):1257–1268, 1978.

[45] S. Baroni, P. Giannozzi, and E. Isaev. Density-functional perturbation theory for quasi-harmonic calculations. *Rev. Mineral. Geochem.*, 71(1): 39–57, 2010.

[46] T. Dengg, V. Razumovskiy, L. Romaner, G. Kresse, P. Puschnig, and J. Spitaler. Thermal expansion coefficient of WRe alloys from first principles. *Phys. Rev.*, 96(3):035148, 2017.

[47] D. Music, S. Khayyamifar, and J. Hektor. Conflicting primary and secondary properties of thermoelectric devices–a case study on the thermomechanical behavior of ZrNiSn. *Comp. Mater. Sci.*, 230:112530, 2023.

[48] V. L. Moruzzi, J. F. Janak, and K. Schwarz. Calculated thermal properties of metals. *Phys. Rev. B*, 37(2):790, 1988.

[49] P. Söderlind, L. Nordström, L. Yongming, and B. Johansson. Relativistic effects on the thermal expansion of the actinide elements. *Phys. Rev. B*, 42 (7):4544, 1990.

[50] V.A. Drebushchak. Thermal expansion of solids: review on theories. *Journal of Thermal Analysis and Calorimetry*, 142(2):1097–1113, 2020.

[51] J. C. Slater. *Introduction to chemical physics*. Read Books Ltd, 2011.

[52] P. Hiremath. *Grain boundary embrittlement due to phosphorus in tungsten: An atomistic approach*. Lund University, 2024.

[53] J. R. Rice. Dislocation nucleation from a crack tip: an analysis based on the Peierls concept. *J. Mech. Phys. Solids*, 40(2):239–271, 1992.

[54] P. M. Kelly, H.-P. Ren, D. Qiu, and M.-X. Zhang. Identifying close-packed planes in complex crystal structures. *Acta Mater.*, 58:3091–3095, 2010.

[55] A. Vesti, P. Hiremath, S. Melin, and P. A. T. Olsson. Ab-initio investigation of mechanical and fracture-related properties of W-Re σ and χ precipitates. *J. Nucl. Mater.*, page 154261, 2023.

[56] Kyosuke Kishida, Masaomi Okutani, and Haruyuki Inui. Direct observation of zonal dislocation in complex materials by atomic-resolution scanning transmission electron microscopy. *Acta Materialia*, 228:117756, 2022.

[57] Kyosuke Kishida, Masaomi Okutani, Hirotaka Suzuki, Haruyuki Inui, Martin Heilmaier, and Dierk Raabe. Room-temperature deformation of single crystals of the sigma-phase compound fecr with the tetragonal d8b structure investigated by micropillar compression. *Acta Materialia*, 249:118829, 2023.

[58] P. Hiremath, S. Melin, E. Bitzek, and P.A.T. Olsson. Effects of interatomic potential on fracture behaviour in single-and bicrystalline tungsten. *Comp. Mater. Sci.*, 207:111283, 2022.

[59] J.-M. Joubert and J.-C. Crivello. Non-stoichiometry and Calphad modeling of Frank-Kasper phases. *Appl. Sci.*, 2(3):669–681, 2012.

[60] S. G. Fries and B. Sundman. Using Re-W σ-phase first-principles results in the Bragg-Williams approximation to calculate finite-temperature thermodynamic properties. *Phys. Rev. B*, 66(1):012203, 2002.

[61] J. C. Crivello and J. M. Joubert. First principles calculations of the σ and χ phases in the Mo-Re and W-Re systems. *J. Phys.: Condens. Matter*, 22: 035402, 2009.

[62] G. Bonny, A. Bakaev, D. Terentyev, and Y. A. Mastrikov. Elastic properties of the sigma W-Re phase: A first principles investigation. *Scr. Mater.*, 128: 45–48, 2017.

[63] C. Berne, A. Pasturel, M. Sluiter, and B. Vinet. Ab initio study of metastability in refractory metal based systems. *Phys. Rev. Lett.*, 83(8):1621, 1999.

[64] B. Seiser, T. Hammerschmidt, A. N. Kolmogorov, R. Drautz, and D. G. Pettifor. Theory of structural trends within 4 d and 5 d transition metal topologically close-packed phases. *Phys. Rev.*, 83(22):224116, 2011.

[65] W. Liu, X.-G. Lu, P. Boulet, and M.-C. Record. Influencing factors of atomic order in the binary sigma phase. *Intermetallics*, 93:6–19, 2018.

[66] W. Liu, X.-G. Lu, Q.-M. Hu, H. Wang, Y. Liu, P. Boulet, and M.-C. Record. Atomic bonding and electronic stability of the binary sigma phase. *J. Alloys Compd.*, 811:152053, 2019.

[67] E. Clementi, D. L. Raimondi, and W. P. Reinhardt. Atomic screening constants from SCF functions. II. Atoms with 37 to 86 electrons. *J. Chem. Phys.*, 47(4):1300–1307, 1967.

[68] The MathWorks Inc. What is a support vector machine?, 2022. URL `https://www.mathworks.com/help/stats/index.html`.

[69] Z.-P. Zhu, D. Jia, W. Y. Wang, J.-L. Yin, X.-Y. Gao, S.-F. Yang, H.-F. Song, and J.-S. Li. Effect of order–disorder transition on thermodynamic and electronic properties of σ and χ phases in W–Re alloy: the first-principles calculation. *Tungsten*, pages 1–19, 2024.

[70] X.-Q. Chen, H. Niu, D. Li, and Y. Li. Modeling hardness of polycrystalline materials and bulk metallic glasses. *Intermetallics*, 19(9):1275–1281, 2011.

[71] L. A. Gypen and A. Deruyttere. The combination of atomic size and elastic modulus misfit interactions in solid solution hardening. *Scr. Metall.*, 15(8): 815–820, 1981.

[72] E. Nembach. Precipitation hardening caused by a difference in shear modulus between particle and matrix. *Phys. Status Solidi A*, 78(2):571–581, 1983.

[73] R. E. Smallman and A. H. W. Ngan. *Modern Physical Metallurgy*. Elsevier, 2014.

[74] G. Bonny, A. Bakaev, and D. Terentyev. Assessment of hardening due to non-coherent precipitates in tungsten-rhenium alloys at the atomic scale. *Sci. Rep.*, 9:2045–2322, 2019.

[75] Y. R. Sharapova, A. M. Kazakov, E. A. Korznikova, A. Zinovev, D. Terentyev, and S. V. Dmitriev. Effect of temperature and rhenium content in precipitates on dispersion hardening of tungsten. *Karbala Int. J. Mod. Sci.*, 11(1):3, 2024.

[76] Y. Yanagi, Y. Yamakawa, N. Adachi, and Y. Ōno. Orbital order, structural transition, and superconductivity in iron pnictides. *J. Phys. Soc. Jpn.*, 79 (12):123707, 2010.

[77] H. Kontani, T. Saito, and S. Onari. Origin of orthorhombic transition, magnetic transition, and shear-modulus softening in iron pnictide superconductors: Analysis based on the orbital fluctuations theory. *Phys. Rev. B*, 84(2):024528, 2011.

[78] S. Harikrishnan, S. Rößler, C. M. N. Kumar, H. L. Bhat, U. K. Rößler, S. Wirth, F. Steglich, and S. Elizabeth. Phase transitions and rare-earth magnetism in hexagonal and orthorhombic $DyMnO_3$ single crystals. *J. Phys.: Condens. Matter*, 21(9):096002, 2009.

[79] T. Goto, T. Kimura, G. Lawes, A. P. Ramirez, and Y. Tokura. Ferroelectricity and giant magnetocapacitance in perovskite rare-earth manganites. *Phys. Rev. Lett.*, 92(25):257201, 2004.

[80] H. A. Jahn and E. Teller. Stability of polyatomic molecules in degenerate electronic states I–Orbital degeneracy. *Proc. R. Soc. London, Ser. A*, 161 (905):220–235, 1937.

[81] J. S. Cantrell, R. C. Jr. Bowman, and D. B. Sullenger. X-ray diffraction and nuclear magnetic resonance studies of the relationship between electronic structure and the tetragonal distortion in zirconium hydride (ZrH_x). *J. Phys. Chem.*, 88(5):918–923, 1984.

[82] M. Gupta. Electronically driven tetragonal distortion in TiH_2. *Solid State Commun.*, 29(1):47–51, 1979.

[83] P. A. T. Olsson, A. R. Massih, J. Blomqvist, A.-M. A. Holston, and C. Bjerkén. Ab initio thermodynamics of zirconium hydrides and deuterides. *Comput. Mater. Sci.*, 86:211–222, 2014.

[84] P. A. T. Olsson, J. Blomqvist, C. Bjerkén, and A. R. Massih. Ab initio thermodynamics investigation of titanium hydrides. *Comput. Mater. Sci.*, 97:263–275, 2015.

[85] J. B. Conway. Properties of some refractory metals. III. thermal expansion characteristics of tungsten, rhenium, tantalum, molybdenum, niobium,

W-25Re, Ta-10W, and Mo-50Re. Technical report, General Electric Co., Cincinnati, Ohio. Nuclear Materials and Propulsion, 1965.

[86] K. Wang and R. R. Reeber. The role of defects on thermophysical properties: thermal expansion of V, Nb, Ta, Mo and W. *Mater. Sci. Eng.: R: Rep.*, 23(3):101–137, 1998.

[87] P. Söderlind and B. Johansson. Calculated thermal expansion of d and f transition metals. *Thermochim. Acta*, 218:145–153, 1993.

[88] M. H. Manghnani, K. Katahara, and E. S. Fisher. Ultrasonic equation of state of rhenium. *Phys. Rev.*, 9(4):1421, 1974.

[89] C.-R. Xu, L. Shao, N. Ding, H.-H. Jiang, and B.-Y. Tang. Study of thermal properties of TiCN by Debye Einstein model, Debye Grüneisen model and quasiharmonic approximation. *Physica B*, 674:415589, 2024.

[90] V. G. Andrianova, A. Z. Zhuk, V. M. Ziachenko, E. B. Zaretskii, V. A. Petukhov, and V. Y. Chekhovskoi. Anomalous concentration dependence of some physical properties of tungsten-rhenium alloys. *High Temperature*, 21(1):70–75, 1983.

[91] A. Vesti, D. Music, and P. A. T. Olsson. First-principles study on thermal expansion of W-Re sigma and chi phases. *Nucl. Mat. Energy*, page 101684, 2024.

[92] I. Steinbach. Phase-field models in materials science. *Modell. Simul. Mater. Sci. Eng.*, 17(7):073001, 2009. doi: 10.1088/0965-0393/17/7/073001.

[93] O. C. Zienkiewicz, R. L. Taylor, and J. Zhu. *The Finite Element Method: Its Basis and Fundamentals*. Elsevier, 7 edition, 2013. doi: 10.1016/C2009-0-21561-1.

[94] Ralf Drautz. Atomic cluster expansion for accurate and transferable interatomic potentials. *Physical Review B*, 99(1):014104, 2019.

[95] Yury Lysogorskiy, Cas van der Oord, Anton Bochkarev, Sarath Menon, Matteo Rinaldi, Thomas Hammerschmidt, Matous Mrovec, Aidan Thompson, Gábor Csányi, Christoph Ortner, et al. Performant implementation of the atomic cluster expansion (pace) and application to copper and silicon. *npj computational materials*, 7(1):97, 2021.

[96] Genevieve Dusson, Markus Bachmayr, Gábor Csányi, Ralf Drautz, Simon Etter, Cas van Der Oord, and Christoph Ortner. Atomic cluster expansion: Completeness, efficiency and stability. *Journal of Computational Physics*, 454:110946, 2022.

Scientific publications

Author's contribution statement

Co-authors are abbreviated as follows:
Pär A. T. Olsson (PO), Praveenkumar Hiremath (PH), Solveig Melin (SM), Denis Music (DM), Thomas Hammerschmidt (TH), Mauro Palumbo (MP).

Paper I: *Ab-initio* investigation of mechanical and fracture-related properties of W–Re σ and χ precipitates

The idea of the paper was conceived in discussion with my co-authors. I performed the simulations and data analysis, and wrote the original draft. PH assisted with the fracture-related calculations. PO and SM assisted in reviewing and editing the manuscript.

Paper II: First-principles study on thermal expansion of W–Re sigma and chi phases

The idea of the paper was conceived in discussion with my co-authors. I performed the simulations and data analysis, and wrote the original draft. PO and DM assisted in reviewing and editing the manuscript.

Paper III: Impact of composition and lattice site occupancy on mechanical stability and fracture-related properties in W-Os sigma phase

The idea of the paper was conceived in discussion with my co-authors. I performed the simulations and data analysis, and wrote the original draft. PO, DM, TH, and MP assisted in reviewing and editing the manuscript.

Paper IV: First-principles study of dynamic instability and phase transformation in the W–Re and W–Os sigma phase

The idea of the paper was conceived in discussion with my co-authors. I performed the simulations and data analysis, and wrote the original draft. PO, DM, TH, and MP assisted in reviewing and editing the manuscript.